

Spatio-temporal areal models to support small area estimation: An application to national-scale forest carbon monitoring

Elliot S. Shannon^{1, 2}, Andrew O. Finley^{1, 2}, Paul B. May³,
Grant M. Domke⁴, Hans-Erik Andersen⁵, George C. Gaines, III⁶, Sudipto Banerjee⁷

1. Department of Forestry, Michigan State University, East Lansing, MI, USA.
2. Department of Statistics and Probability, Michigan State University, East Lansing, MI, USA.
3. Department of Mathematics, South Dakota School of Mines and Technology, Rapid City, SD, USA.
4. USDA Forest Service, Northern Research Station, St. Paul, MN, USA.
5. USDA Forest Service, Pacific Northwest Research Station, Seattle, WA, USA.
6. USDA Forest Service, Rocky Mountain Research Station, Missoula, MT, USA.
7. Department of Biostatistics, University of California, Los Angeles, Los Angeles, CA, USA.

Corresponding Author: Elliot S. Shannon, email: shann125@msu.edu.

Abstract

1. National Forest Inventory (NFI) programs can provide vital information on the status, trend, and change in forest parameters. These programs are being increasingly asked to provide forest parameter estimates for spatial and temporal extents smaller than their current design and accompanying design-based methods can deliver with desired levels of uncertainty. Many NFI designs and estimation methods focus on status and are not well equipped to provide acceptable estimates for trend and change parameters, especially over small spatial domains and/or short time periods.
2. Fine-scale space-time indexed estimates are critical to a variety of environmental, ecological, and economic monitoring efforts. Estimates for forest carbon status, trend, and change are of particular importance to international initiatives to track carbon dynamics. Model-based small area estimation (SAE) methods for NFI and similar ecological monitoring data typically pursue inference on status within small spatial domains, with few demonstrated methods that account for spatio-temporal dependence needed for trend and change estimation.
3. We propose a spatio-temporal Bayesian model framework that delivers statistically valid estimates with full uncertainty quantification for status, trend, and change. The framework accommodates a variety of space and time dependency structures, and we detail model configurations for different settings.

4. Through analysis of simulated datasets, we compare the relative performance of candidate models and a traditional direct estimator. We then apply candidate models to a large-scale NFI dataset to demonstrate the utility of the proposed framework for providing unique quantification of forest carbon dynamics in the contiguous United States. We also provide computationally efficient algorithms, software, and data to reproduce our results and for benchmarking.

1 Introduction

Given the ecological and economic importance of forests, national forest inventory (NFI) programs have been implemented to perform large-scale forest monitoring. Data generated by these programs offer a unique and powerful resource for determining the extent, magnitude, and causes of long-term changes in forest health, timber resources, and forest landowner characteristics (Wurtzebach et al., 2019). Traditionally, NFI programs provide design-based estimates for forest parameters based on measurements taken on a forest inventory plot network (Bechtold and Patterson, 2005; Westfall et al., 2022; Tomppo et al., 2009). Depending on the desired level of estimate precision, such approaches often require repeated costly measurements over a relatively dense inventory plot network; hence, from a cost efficiency standpoint, there is interest in methods that can deliver comparable inference using fewer inventory plots and remeasurements. At the same time, agencies that administer NFIs are experiencing increased demand for estimates within smaller spatial, temporal, and biophysical extents than design-based inference can reasonably deliver (Köhl et al., 2006; Breidenbach and Astrup, 2012; Prisley et al., 2021). Developing estimation methods that support inference on small areas—referred to as small area estimation (SAE)—using NFI data is an active area of research, with considerable progress made in recent years (Hou et al., 2021; Coulston et al., 2021; Schroeder et al., 2014; Lister et al., 2020; Finley et al., 2024). Here, “small area” does not necessarily refer to small spatial extents alone, rather, to any domain of interest that contains too few observations to deliver accurate direct estimates. SAE methods are numerous and diverse, although most seek to improve inference in small areas by leveraging observations from both within and outside the domain of interest, auxiliary information correlated with the outcome variables, and statistical models describing their relationship.

Though inferences on small area parameters may proceed from the probabilistic nature of the sample design (e.g., Breidt and Opsomer 2017; Wojcik et al. 2022; Affleck and Gaines III 2023), most contemporary SAE methods rely on statistical models for inference (Rao and Molina, 2015). Both design- and model-based approaches to small area estimation are well developed and compared in the statistical and forestry/ecology literature (see, e.g., Särndal et al., 1978, 2003; Gregoire, 1998; McRoberts, 2010; Dumelle et al., 2022). The design-based approach assumes a fixed finite population that is accessible (in principle without error) through a census if all population units were observed. Randomness is incorporated via the selection of population units into a sample according to a randomized sampling design. This is often effective when variability and dependence across population units are adequately captured by the sampling design, which assigns a probability of selection to each sample. However, if units in the population exhibit associations or dependencies

that are too complex to be captured by a sampling design or there is a paucity of data, e.g., due to prohibitive collection costs, then a model-based approach might be preferable (see, e.g., the developments in Little, 2004; Ghosh, 2012; Banerjee, 2024, for model-based as well as fully Bayesian perspectives to inference for finite populations). In applications considered here, we assume the population is a realization from a data-generating stochastic process, and hence we pursue model-based SAE.

SAE methods can generally be classified into two groups: unit-level and area-level models. Unit-level models are constructed at the level of population units, which are defined as the minimal units that can be sampled from a population. With respect to most NFI surveys, field plot centers represent population units. Unit-level models typically relate outcome variable measurements on sampled population units to auxiliary data that is available for all population units. Prediction for a small area is achieved by aggregating unit-level predictions within a given areal extent (Rao and Molina, 2015). In contrast, area-level models are constructed across areal units, where relationships are built between area-specific direct estimates (e.g., generated using design-based estimators applied to samples within each area) and auxiliary data (Rao and Molina, 2015). Hence, area-level models effectively “adjust” direct estimates given auxiliary information.

For NFI data indexed in space and time, unit-level models often provide additional flexibility for model specification and benefit from the well developed theory and methods for point-referenced spatio-temporal data (Banerjee et al., 2004; Cressie and Wikle, 2011). Residual spatial and/or temporal dependence in NFI data have been effectively modeled using Gaussian processes (GPs)(see, e.g., Datta et al., 2016; May and Finley, 2024; Finley et al., 2024, that have also focused on scaling analysis to massive datasets). However, if sampling locations are unavailable or data are reported for predefined areas, then area-level models are frequently pursued. Given the often proprietary nature of NFI data, our current work focuses on area-level models, specifically the Fay-Herriot (FH) model (Fay and Herriot, 1979).

FH models incorporate design-based (i.e., direct) estimates, area-specific auxiliary information, and spatio-temporal dependence among areal units to improve inference, and have recently been applied to forest inventory applications (see, e.g., Ver Planck et al., 2018; Temesgen et al., 2021; Cao et al., 2022; Stanke et al., 2022). Working within a hierarchical Bayesian framework, Ver Planck et al. (2018) included conditional autoregressive spatial random effects in a FH model to improve inference for above-ground forest carbon parameters within small areas. This improvement was also shown in Chandra et al. (2015), where regression coefficients varied spatially to accommodate nonstationary spatial dependence. Temesgen et al. (2021) demonstrated a FH model’s utility in operational forestry by coupling field and remotely sensed data to improve stand-level estimates. More recently, May et al. (2023) developed a Bayesian FH model to estimate forest above-ground biomass density across the contiguous United States (CONUS). Their work identified useful remotely sensed auxiliary predictor variables and advantages to modeling nonstationary relationships using spatially-varying regression coefficients.

Given that NFI data often cover large spatial extents and temporally dynamic forest and land use systems, posited models should accommodate spatial-temporal dependence. This dependence should likely extend beyond space- and time-varying intercepts to accommodate nonstationary relationships between the outcome and predictor variables (as shown in May

et al., 2023; Finley et al., 2011; Datta et al., 2016; May and Finley, 2024). There is a rich literature on spatio-temporal area-level models, much of which originates from public health research (see, e.g., Waller et al., 1997; Rushworth et al., 2014, 2017; Lee et al., 2018). There are, however, few examples of spatio-temporal FH models. Rao and Yu (1994) extended a FH model to accommodate time-series data, although spatial dependence was not considered. More recently, Marhuenda et al. (2013) developed a spatio-temporal FH model for income data in Spain, where the model incorporated a space- and time-varying intercept.

We intend to provide useful inference for key forest parameters in small areas that cannot be reliably obtained using design-based methods. To this end, we develop a spatio-temporal Bayesian FH model capable of delivering statistically valid estimates with full uncertainty quantification for: 1) annual parameters (e.g., status at a given time); 2) trend (e.g., average change over some time interval); and 3) change (e.g., difference between two points in time). The model and approach to parameter estimation were chosen to accommodate features common in NFI data, including: 1) spatial and temporal dependence across areal units; 2) nonstationary relationships with area-level predictor variables; and 3) missing direct estimates due to the often extremely small spatial and temporal extents. Here, too, we provide computationally efficient parameter estimation algorithms and associated code for implementation. A simulation study is used to assess the proposed model-based estimator, along with its submodels, and compare them with a design-based direct estimator. Finally, the proposed model and submodels are applied to United States Department of Agriculture (USDA) Forest Service NFI data to quantify annual status, trend, and change estimates in county-level carbon density and totals across the CONUS over 14 years.

The remainder of the paper is structured as follows. In Section 2, we discuss aspects of NFI data, define the proposed model and submodels, and outline their implementation. The simulation and FIA data analyses are presented in Section 3. Results are given in Section 4 along with a discussion about strengths and weaknesses of the proposed FH model for application in NFI.

2 Methods

2.1 Direct Estimators

Here, we consider spatio-temporal NFI survey data that are collected for a design-based inventory system, where individual inventory plots are repeatedly measured within nonoverlapping discrete areal units and time steps. Specifically, let $y_{i,j,t}$ be the measurement for the i^{th} sampling unit in areal unit j at time t , where $i = 1, \dots, n_{j,t}$ indexes sampling units, $j = 1, \dots, J$ indexes areal units, and $t = 1, \dots, T$ indexes time steps. Hence, $n_{j,t}$ is the total number of sampling units measured in areal unit j at time t . Our goal is to learn about a latent parameter of interest, denoted $\mu_{j,t}$, which is the population mean for areal unit j at time t . In the SAE setting, the $n_{j,t}$ are too small to produce estimates with desired levels of accuracy, but design-based direct estimates may still be calculated and used to inform the subsequent model-based estimate for $\mu_{j,t}$ presented in Section 2.2. The design-based direct

estimate for $\mu_{j,t}$ is calculated as

$$\hat{\mu}_{j,t} = \frac{1}{n_{j,t}} \sum_{i=1}^{n_{j,t}} y_{i,j,t}. \quad (1)$$

where the estimate variance for (1) is

$$\hat{\sigma}_{j,t}^2 = \frac{1}{n_{j,t}(n_{j,t} - 1)} \sum_{i=1}^{n_{j,t}} (y_{i,j,t} - \hat{\mu}_{j,t})^2. \quad (2)$$

Often, the areal and/or temporal extent is especially small, and few or no plot measurements are available (i.e., $n_{j,t} \in \{0, 1\}$), leading to missing direct estimates $\hat{\mu}_{j,t}$ and/or $\hat{\sigma}_{j,t}^2$. Additionally, when plot measurements in areal unit j at time t are identical, $\hat{\sigma}_{j,t}^2$ will be equal to 0. In these cases, we still would like the SAE model to produce an estimate for $\mu_{j,t}$.

2.2 Model

We hope to learn about $\mu_{j,t}$ from its direct estimate $\hat{\mu}_{j,t}$, its associated variance statistic $\hat{\sigma}_{j,t}^2$, and from information borrowed from direct estimates for adjacent areas proximate in space and time. Further, we might glean information about $\mu_{j,t}$ from relationships between $\hat{\mu}_{j,t}$ and area-level predictors. Given the large spatial and temporal extents of NFI data, we expect the impact of these predictors to be nonstationary over space and/or time. Since we consider only discrete space and time, we employ autoregressive structures to capture spatial and temporal correlation. Spatial correlations are usually modeled through structures such as conditional (CAR) or simultaneous (SAR) autoregressive models (Banerjee et al., 2004; Ver Hoef et al., 2018). Similarly, temporal correlations are modeled using autoregressive or dynamic structures. Incorporating spatial and/or temporal correlations in these ways could further improve model estimates for $\mu_{j,t}$, especially in cases where direct estimates are imprecise or missing.

The model we propose is an extension to the traditional FH model to accommodate spatio-temporal data of the form described above. For areal unit j at time t the model is

$$\hat{\mu}_{j,t} = \mu_{j,t} + \delta_{j,t}, \quad (3)$$

$$\mu_{j,t} = \beta_0 + \eta_{0,j,t} + \sum_{k=1}^p x_{k,j,t} \beta_k + \sum_{k=1}^q \tilde{x}_{k,j,t} \eta_{k,j,t} + \epsilon_{j,t}, \quad (4)$$

where $\delta_{j,t}$ and $\epsilon_{j,t}$ are mutually exclusive error terms distributed as mean zero normal (N) distributions with $\delta_{j,t} \stackrel{ind}{\sim} N(0, \sigma_{\delta,j,t}^2)$ and $\epsilon_{j,t} \stackrel{iid}{\sim} N(0, \sigma_{\epsilon}^2)$. The regression component in (4) comprises a customary fixed effects regression component $\beta_0 + \sum_{k=1}^p x_{k,j,t} \beta_k$ and a spatio-temporally varying regression component $\eta_{0,j,t} + \sum_{k=1}^q \tilde{x}_{k,j,t} \eta_{k,j,t}$. Each $x_{k,j,t}$, for $k = 1, \dots, p$, represents a predictor (or explanatory) variable referenced for each areal unit j and time t that comprises the fixed effects regression and $\tilde{x}_{k,j,t}$ represents one of $q \leq p$ predictor variables included in the spatio-temporally varying component of the model. The restriction $q \leq p$ is not essential, but customary in spatio-temporally varying coefficient models since the $\tilde{x}_{k,j,t}$'s are usually a subset of the $x_{k,j,t}$'s. A Bayesian specification will be completed with prior

distributions on all these parameters, where $\eta_{0,j,t}$ and $\eta_{k,j,t}$'s will each be endowed with a spatio-temporal distribution.

As defined in (1), the design-unbiased estimate for $\mu_{j,t}$, i.e., $\hat{\mu}_{j,t}$, is based on the survey design and is assumed to provide information about the true, but latent, mean. Traditionally in FH model applications, the design-based sampling-error variance $\hat{\sigma}_{j,t}^2$ estimate, defined in (2), is set as the variance of $\delta_{j,t}$ (see, e.g., Wang et al., 2012; Porter et al., 2014; Rao and Molina, 2015). This, however, can have undesirable inferential consequences as exposed by substituting the expression for $\mu_{j,t}$ in (4) into (3). The resulting residual variance is $\text{var}(\epsilon_{j,t} + \delta_{j,t}) = \text{var}(\epsilon_{j,t}) + \hat{\sigma}_{j,t}^2$, where the latter term is now a fixed constant. The estimate for this residual variance depends on the least squares estimates for β_0 , β_k 's, $\eta_{0,j,t}$, and $\eta_{k,j,t}$'s that, in turn, depend upon the predictor variables in (4). There appears to be no theoretical assurance that these predictor variables will indeed provide a residual variance estimate that is greater than the fixed estimate $\hat{\sigma}_{j,t}^2$. It seems, then, possible that the estimate for $\text{var}(\epsilon_{j,t})$ could be forced to be zero (since it cannot be negative) as a purely numerical consequence of fixing a variance component rather than allowing the data to estimate it.

Instead, we prefer to incorporate information from the design-based estimate by modeling this variance parameter as an inverse-Gamma (*IG*) random variable $\sigma_{j,t}^2 \sim IG\left(\frac{n_{j,t}}{2}, \frac{(n_{j,t}-1)\hat{\sigma}_{j,t}^2}{2}\right)$. Modeling $\sigma_{j,t}^2$ in this way allows us to more clearly obtain potential information from the observed sample size $n_{j,t}$. Specifically, as $n_{j,t}$ increases, the mean of $\sigma_{j,t}^2$ concentrates near $\hat{\sigma}_{j,t}^2$ and its precision increases.

We now turn to the specifications for spatial and temporal random effects. Following (4), a given specification will have $(q + 1)$ random effects vectors, one for the intercept and q for those predictor variables for which we posit there are space- and/or time-varying relationships with the outcome. Here, we develop specifications for one vector of random effects, and then generalize to $(q + 1)$ when connecting them to (4). We define a $J \times 1$ vector of spatial random effects as

$$\boldsymbol{\eta}^s \sim MVN(\mathbf{0}, \sigma_{\eta^s}^2 \mathbf{R}(\rho_{\eta^s})), \quad (5)$$

where the s superscript on $\boldsymbol{\eta}$ indicates these are the spatial effects following a mean zero multivariate Normal (*MVN*) distribution with covariance matrix $\sigma_{\eta^s}^2 \mathbf{R}(\rho_{\eta^s})$. Here, and in subsequent notation, bold font indicates a vector or matrix. In this specification, $\sigma_{\eta^s}^2$ is the scalar variance, ρ_{η^s} is the correlation parameter, and $\mathbf{R}(\rho_{\eta^s}) = (\mathbf{D} - \rho_{\eta^s} \mathbf{W})^{-1}$ is the $J \times J$ correlation matrix reflecting a CAR spatial structure, as specified in Banerjee et al. (2004). Here, \mathbf{W} is the $J \times J$ binary spatial adjacency matrix with elements $w_{ij} = 1$ if areal units i and j are neighbors and $w_{ij} = 0$ otherwise, with $w_{ii} = 0$. In addition, \mathbf{D} is a $J \times J$ diagonal matrix with i^{th} diagonal element s_i , where s_i is the total number of neighbors adjacent to areal unit i , with $s_i \geq 1$. While we define the CAR model and subsequent random effects using the covariance matrix, estimation algorithms work with the precision matrix because it yields certain computational advantages detailed in Section 2.5.

When collecting all $N = JT$ space and time observations, we stack by areal units such that the first T elements correspond to areal unit 1 at time points $1, \dots, T$, and the last T elements correspond to areal unit J at time points $1, \dots, T$. We then define an $N \times 1$ vector of area-specific temporal random effects as

$$\boldsymbol{\eta}^t \sim MVN(\mathbf{0}, \sigma_{\eta^t}^2 \mathbf{I} \otimes \mathbf{A}(\alpha_{\eta^t})), \quad (6)$$

where the t superscript on $\boldsymbol{\eta}$ indicates these are temporal effects, $\sigma_{\eta^t}^2$ is a scalar variance, \mathbf{I} is a $J \times J$ identity matrix, \otimes is the Kronecker product operator, and $\mathbf{A}(\alpha_{\eta^t})$ is a $T \times T$ first order autoregressive correlation matrix with temporal correlation parameter α_{η^t} and ij^{th} element equal to $\alpha_{\eta^t}^{|i-j|}$. Finally, the $N \times 1$ vector of spatial-temporal random effects is

$$\boldsymbol{\eta}^{st} \sim MVN(\mathbf{0}, \sigma_{\eta^{st}}^2 \mathbf{R}(\rho_{\eta^{st}}) \otimes \mathbf{A}(\alpha_{\eta^{st}})), \quad (7)$$

where $\boldsymbol{\eta}^{st}$ indicates these are spatio-temporal effects, $\sigma_{\eta^{st}}^2$ is a scalar variance, and remaining terms have been defined earlier. Hence, the area-specific spatial effect evolves over time.

In subsequent analyses, we consider the following candidate models for $\mu_{j,t}$.

$$\text{Full model: } \mu_{j,t} = \beta_0 + \eta_{0,j,t}^{st} + \sum_{k=1}^p x_{k,j,t} \beta_k + \sum_{k=1}^q \tilde{x}_{k,j,t} \eta_{k,j}^s + \epsilon_{j,t} \quad (8)$$

$$\text{Submodel 1: } \mu_{j,t} = \beta_0 + \eta_{0,j,t}^{st} + \sum_{k=1}^p x_{k,j,t} \beta_k + \epsilon_{j,t} \quad (9)$$

$$\text{Submodel 2: } \mu_{j,t} = \beta_0 + \eta_{0,j,t}^t + \sum_{k=1}^p x_{k,j,t} \beta_k + \epsilon_{j,t} \quad (10)$$

As described later in Section 3, our current setting displays no evidence of predictor variables $\tilde{x}_{k,j,t}$'s having time-varying impact, hence our full model stops short of specifying spatio-temporal coefficients and considers only space-varying coefficients (SVCs). In other settings, one might consider a $\eta_{k,j,t}^{st}$ associated with some or all $\tilde{x}_{k,j,t}$'s. One might also define a submodel with a space-varying intercept; here, however, because we have repeated measurements and are interested in trend and change within each areal unit, we acknowledge temporal dependence since a space-varying intercept alone would not be adequate.

2.3 Parameter estimation and inference

To complete the Bayesian model specification, we assign prior distributions to the model parameters. For the full model (8), the joint posterior distribution for all parameters is

$$\begin{aligned} & \prod_{j=1}^J \prod_{t=1}^T N(\hat{\mu}_{j,t} | \mu_{j,t}, \sigma_{j,t}^2) \times \prod_{j=1}^J \prod_{t=1}^T N\left(\mu_{j,t} | \beta_0 + \eta_{0,j,t}^{st} + \sum_{k=1}^p x_{k,j,t} \beta_k + \sum_{k=1}^q \tilde{x}_{k,j,t} \eta_{k,j}^s, \sigma_{\epsilon}^2\right) \times \\ & \prod_{k=0}^p N(\beta_k | \mu_{\beta}, \sigma_{\beta}^2) \times \prod_{j=1}^J \prod_{t=1}^T IG\left(\sigma_{j,t}^2 | \frac{n_{j,t}}{2}, \frac{(n_{j,t} - 1) \hat{\sigma}_{j,t}^2}{2}\right) \times IG(\sigma_{\epsilon}^2 | a_{\epsilon}, b_{\epsilon}) \times \\ & MVN(\boldsymbol{\eta}_0^{st} | \mathbf{0}, \sigma_{\eta^{st}}^2 \mathbf{R}(\rho_{\eta^{st}}) \otimes \mathbf{A}(\alpha_{\eta^{st}})) \times \\ & IG(\sigma_{\eta_0^{st}}^2 | a_{\eta_0^{st}}, b_{\eta_0^{st}}) \times U(\rho_{\eta_0^{st}} | a_{\rho}, b_{\rho}) \times U(\alpha_{\eta_0^{st}} | a_{\alpha}, b_{\alpha}) \times \\ & \prod_{k=1}^q MVN(\boldsymbol{\eta}_k^s | \mathbf{0}, \sigma_{\eta_k^s}^2 \mathbf{R}(\rho_{\eta_k^s})) \times \prod_{k=1}^q IG(\sigma_{\eta_k^s}^2 | a_{\eta_k^s}, b_{\eta_k^s}) \times \prod_{k=1}^q U(\rho_{\eta_k^s} | a_{\rho}, b_{\rho}). \end{aligned} \quad (11)$$

Here, the normal prior distribution mean μ_{β} and variance σ_{β}^2 for elements in $\boldsymbol{\beta}$ were set at 0 and 10^5 , respectively. With the exception of the IG prior for $\sigma_{j,t}^2$ described in Section 2.2,

each scalar variance parameter was assigned an *IG* prior with a shape $a = 2$ and scale b set based on exploratory analysis. With a shape of 2, the *IG* has an infinite variance and mean centered on the scale parameter. The lower and upper bounds for uniform (*U*) prior distributions on the first order autoregressive parameters α and CAR correlation parameters ρ were set to 0 and 1, respectively.

Parameter inference was based on Markov chain Monte Carlo (MCMC) samples from posterior distributions. With the exception of the correlation parameters α and ρ , closed form full conditional distributions are available for all parameters, and hence we sample from the posterior distributions using Gibbs steps. A Metropolis algorithm is used to sample correlation parameters' posterior distributions. Sampling algorithm details are given in Section 2.5. As reported in Section 3, posterior inference is based on $M = 6,000$ post-convergence and thinned samples from three MCMC chains, i.e., 2,000 from each chain. We use convergence diagnostics and thinning rules outlined in Gelman et al. (2013). Point and interval summaries for model parameters presented in Section 3 include posterior means, medians, and 95% credible intervals.

Along with the latent mean $\mu_{j,t}$, we are interested in its temporal trend and change within and among areal units. Importantly, capturing the temporal correlation in the latent mean within areal units is key to generating statistically valid trend and change parameter estimates. An intuitive measure of trend is the linear least squares slope fit to the latent means over time, which is computed for the j^{th} areal unit as

$$\theta_j = \frac{\sum_{t=1}^T (t - \bar{t}) (\mu_{j,t} - \bar{\mu}_j)}{\sum_{t=1}^T (t - \bar{t})^2}, \quad (12)$$

where $\bar{t} = \frac{1}{T} \sum_{t=1}^T t$ and $\bar{\mu}_j = \frac{1}{T} \sum_{t=1}^T \mu_{j,t}$. Posterior inference about θ_j is accessible using

$$\theta_j^l = \frac{\sum_{t=1}^T (t - \bar{t}) (\mu_{j,t}^l - \bar{\mu}_j^l)}{\sum_{t=1}^T (t - \bar{t})^2}, \quad (13)$$

where l indexes posterior samples $l = 1, 2, \dots, M$. In this way, one sample from $\mu_{j,t}$'s posterior distribution yields one sample from θ_j 's distribution. Given these posterior samples, we can estimate the trend's direction and strength, and perform hypothesis tests, whereby strong support for a non-zero linear trend occurs when the 95% credible interval for θ_j 's posterior distribution does not include zero.

In the same manner, we obtain estimates for change in the latent mean between two time points t_1 and t_2 within areal unit j as

$$\Delta_j = \mu_{j,t_2} - \mu_{j,t_1}. \quad (14)$$

Then, we obtain posterior samples $\Delta_j^l = \mu_{j,t_2}^l - \mu_{j,t_1}^l$ for each $l = 1, 2, \dots, M$.

Given an areal unit's density estimate and area, an estimate for the unit's total is generated. Specifically, for $\mu_{j,t}$ expressed on a per unit area basis, with A_j being the known area of the j^{th} areal unit, we calculate $\Omega_{j,t} = A_j \mu_{j,t}$ as our estimate for the total in areal unit j at time t . Similarly, if trend and change parameters are expressed as densities per unit area, then their totals are $A_j \theta_j$ and $A_j \Delta_j$, respectively. As described above, we can collect samples from the posterior distributions of these total parameters.

Thus far we have considered estimates for individual areal units. However, density, total, trend, and change estimates are easily generated for an arbitrary aggregate of areal units, denoted as $\mathcal{J} \subseteq \{1, \dots, J\}$. Samples from the posterior distribution of an aggregate's total, $\Omega_{\mathcal{J},t}$ are obtained simply as

$$\Omega_{\mathcal{J},t}^l = \sum_{j \in \mathcal{J}} A_j \mu_{j,t}^l. \quad (15)$$

Given (15), one can sample from the aggregate's density $\mu_{\mathcal{J},t}$ posterior distribution using

$$\mu_{\mathcal{J},t}^l = \frac{\Omega_{\mathcal{J},t}^l}{A_{\mathcal{J}}}, \quad (16)$$

where $A_{\mathcal{J}} = \sum_{j \in \mathcal{J}} A_j$.

Further, aggregate trend $\theta_{\mathcal{J}}$ and change $\Delta_{\mathcal{J}}$ parameters are sampled via

$$\theta_{\mathcal{J}}^l = \frac{\sum_{t=1}^T (t - \bar{t}) (\mu_{\mathcal{J},t}^l - \bar{\mu}_{\mathcal{J}}^l)}{\sum_{t=1}^T (t - \bar{t})^2}, \quad (17)$$

with $\bar{\mu}_{\mathcal{J}}^l = \frac{1}{T} \sum_{t=1}^T \mu_{\mathcal{J},t}^l$, and

$$\Delta_{\mathcal{J}}^l = \mu_{\mathcal{J},t_2}^l - \mu_{\mathcal{J},t_1}^l, \quad (18)$$

respectively. Totals based on trend and change parameters are $A_{\mathcal{J}}\theta_{\mathcal{J}}$ and $A_{\mathcal{J}}\Delta_{\mathcal{J}}$, with samples from the respective posterior distributions collected one-for-one using samples from (17) and (18).

2.4 Model comparison

In subsequent analyses, we compare candidate models using the widely applicable information criterion (WAIC; Watanabe, 2010) as implemented in the `loo` R package (Vehtari et al., 2024). A model's estimate for $\text{WAIC} = -2\widehat{\text{elpd}}_{\text{WAIC}}$ and $\widehat{\text{elpd}}_{\text{WAIC}} = \text{lpd} - \widehat{p}_{\text{WAIC}}$, where lpd is the log pointwise predictive density and $\widehat{p}_{\text{WAIC}}$ is the estimated effective number of parameters. Models with lower WAIC should have better fit to the observed data and yield better out-of-sample prediction. For model comparison, we look to the difference in models' $\widehat{\text{elpd}}_{\text{WAIC}}$ and this difference's standard error estimate, labeled $\widehat{\text{elpd}}_{\text{diff}}$ and $\widehat{\tau}_{\text{diff}}$, respectively, see Vehtari et al. (2017) for details.

2.5 Implementation and computing considerations

Gibbs and Metropolis algorithms, used to sample random effects and their process parameters, require increasingly expensive matrix decompositions as J and/or T become large. However, by working with the CAR model's precision matrix, and not the covariance matrix, we are able to avoid the inversion of the covariance matrix in the Gaussian density. Furthermore, the full conditional distributions for the spatial effects are all closed-form Gaussian and the spectral decomposition of the precision matrix lends itself to additional computational gains. MCMC samplers are written in R (R Core Team, 2023) using sparse matrix routines from the `Matrix` package (Bates et al., 2023). In cases where direct estimates $\hat{\mu}_{j,t}$

and/or $\hat{\sigma}_{j,t}^2$ are missing (see Section 2.1), the corresponding $\mu_{j,t}$ sample is updated from its posterior predictive distribution (4). MCMC sampler details and computing considerations are provided in Section S8.

All results presented are reproducible using the MCMC sampler code, data, and workflow scripts provided as Supporting Information Section S7.

3 Applications

The United Nations Framework Convention on Climate Change (UNFCCC) requires parties to submit annual reports with estimates of economy-wide greenhouse gas (GHG) emissions and removals (UNFCCC, 1992). Guidelines for reporting in this agreement and others like it (e.g., 2015 Paris Agreement) have been established by the Intergovernmental Panel on Climate Change (IPCC, 2019). Core among the guidelines are that GHG inventories include “neither over- nor underestimates so far as can be judged, and in which uncertainties are reduced as far as practicable.” In the United States GHG inventory, the NFI is relied on to produce accurate annual estimates for change in forest parameters such as carbon to meet reporting requirements (Domke et al., 2023). However, countries, including the United States (US), are increasingly seeking to improve the accuracy and precision of inventory estimates at finer spatial and temporal scales to meet inventory requirements and other stakeholder needs. However, the relatively coarse NFI spatio-temporal sampling intensities have limited advances in estimating interannual variability in carbon stocks and stock changes on forest land. Given these challenges, the novelty and importance of estimating temporal components in NFI data for small areas is amplified, and provides further motivation for our proposed model and data application.

We present two applications that make use of NFI data collected and developed by the Forest Inventory and Analysis (FIA) program of the USDA Forest Service. An overview of these data are presented in Section 3.1. The first application considers a simulated population built to mimic FIA data characteristics and used to assess design- and model-based estimator qualities. The second application considers actual FIA annual county-level estimates and explores trend in forest carbon density and change over a 14 year study period across the CONUS.

3.1 FIA NFI data

The FIA program measures and monitors more than 300 thousand forest inventory plots in the CONUS (Bechtold and Patterson, 2005; Westfall et al., 2022). Each year, remeasurements are made at approximately 1/5 or 1/7 of all inventory plots in the eastern US and 1/10 of inventory plots in the west, leading to remeasurement intervals (i.e., inventory cycle lengths) ranging from 5 to 10 years. These data are used to generate design-based estimates for important forest parameters, such as forest carbon densities and totals. Carbon content is estimated using measured tree characteristics and national-scale carbon allometric equations based on a comprehensive database of tree species, characteristics, and spatial patterns, for which species-specific carbon fractions are then applied (Westfall et al., 2023). Here, individual tree above-ground carbon estimates are aggregated at the plot-level and

then expanded to a per hectare basis to express carbon density (Mg/ha). Following notation in Section 2.1, we let $y_{i,j,t}$ represent the estimated carbon density (Mg/ha) for FIA plot i in county j and year t .

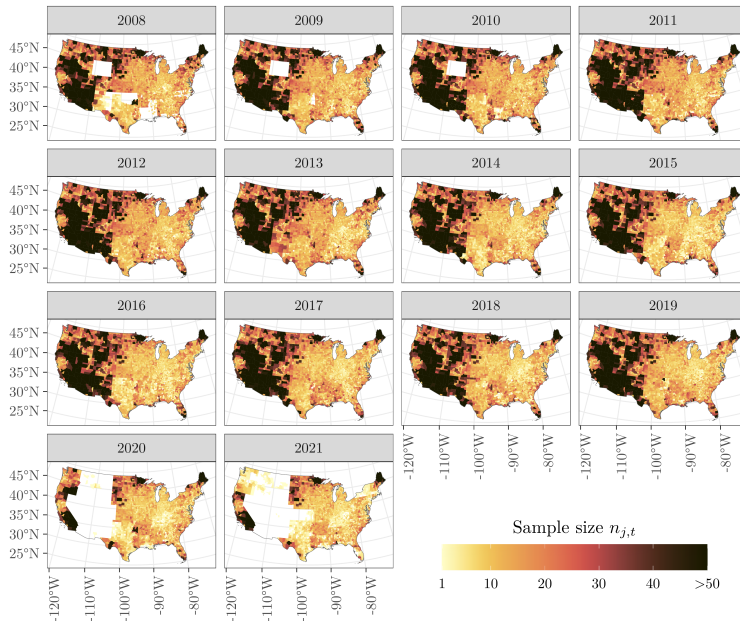


Figure 1: Number of observed FIA plots within each county and year. Transparent counties have zero observed FIA plots.

Here, we consider $J = 3,108$ counties that comprise the CONUS and $T = 14$ years of plot measurements from 2008 to 2021. A county-level map of FIA plot sample size (i.e., $n_{j,t}$) is shown in Figure 1. Only the base intensity plot network, excluding additional intensification plots collected by some states and agencies, is used in our analysis. Of the $N=43,512$ county and time observations, there are 10,627 for which direct estimates are missing. This missingness arises from the absence of measured FIA plots (number of occurrences 1,860), the absence of sampling error variance due to $n_{j,t} = 1$ (820), or the sampling error variance equaling 0 in areal units with only carbon density measurements of zero (7,947). Figure S15 summarizes missingness by county, much of which is concentrated in western and midwestern counties due to lack of forest, survey implementation, and reporting.

Percent tree canopy cover (TCC) data for the CONUS are produced by the USDA Forest Service as part of the National Land Cover Database (NLCD) (Housman et al., 2023). The TCC data are derived from multispectral remote sensing data and have been released as annual maps for years 2008 to 2021 at a 30-by-30 (m) pixel spatial resolution for the CONUS. These data represent fractional pixel-level tree canopy cover expressed as a percentage, which we average for each county and year to produce annual county-level mean TCC (%) shown in Figure 2. For use in subsequent models, this TCC variable was centered and scaled to have mean zero and variance one, and denoted as x_{TCC} where the TCC subscript takes the place of subscript k in models (8-10).

For the analysis of FIA data presented in Section 3.3, interpretation of forest carbon

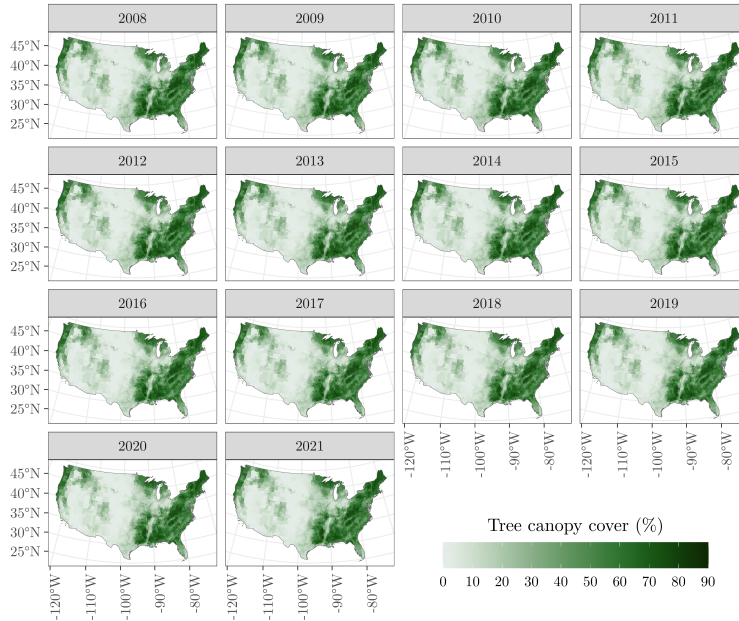


Figure 2: Annual National Land Cover Database percent tree canopy cover averaged within each county.

density estimates comes with a caveat and limitation. The FIA program defines forest land as land which has at least 10% canopy cover of trees of any size, or had at least 10% canopy cover of trees in the past, based on the presence of stumps, snags, or other evidence, and that will be naturally or artificially regenerated. FIA records zero carbon density for non-forest plots, although they could have up to 10% tree canopy cover. Hence, our direct estimate (computed using both forest and non-forest plots) will be negatively biased. Although this bias might be small, difficulty arises when we wish to attribute change in carbon density to change in forest structure and land use—carbon change results from change in forest land area and/or change in carbon density within forest land (e.g., fewer trees). As articulated by Wiener et al. (2021) and Knott et al. (2023), this is a known caveat and limitation when using FIA data for SAE, but also an opportunity for FIA to consider expanding data collection protocols to better support SAE and other model-based estimation efforts.

3.2 Simulation study overview

The simulation study is presented in the Supporting Information Section S5. Here, a single population is generated using fixed and known values for parameters, then estimates for $\mu_{j,t}$, θ_j , and Δ_j are generated from each of a large number of independent samples taken from the population. The four estimators considered are the direct (1), Full model (8), Submodel 1 (9), and Submodel 2 (10). Estimates were compared with the true population parameter values using a set of measures that assess the estimators' bias, accuracy, and precision. The population was simulated to mimic qualities of the observed FIA annual county-level carbon density (Mg/ha) data, with both spatial and temporal dependence. Simulation study results

show that: 1) all estimators are biased when the sample size is small; 2) candidate models yield improved accuracy and uncertainty quantification over the direct estimator; 3) models' IG prior on $\sigma_{j,t}^2$ behaves as expected, weighting the direct estimates according to samples size; 4) WAIC is useful for selecting the candidate model that most closely resembles the data generating model.

3.3 Analysis of FIA NFI data

In this section, we analyze the FIA carbon data described in Section 3.1. Similar to the simulated data analysis, we consider four estimators for the parameter of interest, $\mu_{j,t}$, i.e., direct (1), Full model (8), Submodel 1 (9), and Submodel 2 (10), using direct estimates and x_{TCC} predictor variable values. Given estimates for $\mu_{j,t}$, we also estimate derived parameters θ_j and Δ_j .

As described in Section 1, we anticipated the NFI data to exhibit strong temporal and spatial dependence in the latent mean within and among areal units. This dependence is reflected in the process parameter estimates in Table 1 where temporal and spatial process parameters associated with the model intercept show strong correlation (i.e., $\alpha_{\eta_0^t}$, $\alpha_{\eta_0^{st}}$, and $\rho_{\eta_0^{st}}$ are close to 1) and relatively large variances (i.e., $\sigma_{\eta_0^t}^2$ and $\sigma_{\eta_0^{st}}^2$). For the Full model, the spatial process parameters associated with x_{TCC} , i.e., $\rho_{\eta_{TCC}^s}$ and $\sigma_{\eta_{TCC}^s}^2$, have a strong correlation and relatively large variance.

Considering model fit using WAIC given in Table 1, Submodel 1 has the lowest WAIC, followed by the Full model and then Submodel 2. When testing differences between Submodel 1 and the other candidate models, we see no difference between Submodel 1 and the Full model (i.e., $-15 \pm 1.96 \times 22.2$ includes zero) and Submodel 1 is substantially better than Submodel 2 (i.e., $-642.5 \pm 1.96 \times 51.9$ excludes zero).

As seen in the simulation study presented in Section S5, we again observe varied effects of the prior for $\sigma_{j,t}^2$ on its posterior (Figure S20(a)). This variation reflects increased information about the direct estimate for larger sample sizes, and greater discrepancy between prior and posterior for smaller sample sizes. Similarly, when the sample size is large, posterior estimates for $\mu_{j,t}$ are more similar to the direct estimate $\hat{\mu}_{j,t}$, and when the sample size is small, the posterior estimate is informed by other sources including neighboring direct estimates, predictor variables, and structured random effects (Figure S20(b)). Said differently, when the sample size is small, we express our uncertainty in the direct estimate through the prior, and after observing evidence (i.e., data), our posterior estimate better reflects the information available in the data, which is likely different from the prior. This balance highlights the importance of incorporating prior information when it is available, while acknowledging uncertainty when it is not.

Also discussed in Section 1, given the NFI's large spatial extent that covers many different forest types, environments, and disturbance regimes, we anticipate a nonstationary relationship between tree canopy cover (as captured through x_{TCC}) and carbon density. In other words, we expect the relationship between percent TCC and carbon density to vary spatially over the CONUS. In addition, estimates for the Full model's $\rho_{\eta_{TCC}^s}$ and $\sigma_{\eta_{TCC}^s}^2$ in Table 1 do suggest long-range spatial dependence and substantial variability of η_{TCC}^s , reflecting the mixture of underlying environmental and ecological processes that drive spatial

Parameter	Candidate models		
	Submodel 2	Submodel 1	Full model
β_0	18.15 (17.92, 18.38)	18.39 (18.00, 18.79)	13.83 (12.48, 15.13)
β_{TCC}	15.27 (15.04, 15.53)	18.43 (18.16, 18.83)	16.08 (15.05, 17.18)
$\alpha_{\eta_0^t}$	0.9982 (0.9979, 0.9985)	-	-
$\sigma_{\eta_0^t}^2$	75.73 (71.61, 80.29)	-	-
$\rho_{\eta_0^{st}}$	-	0.9995 (0.9990, 0.9998)	0.9996 (0.9993, 0.9998)
$\alpha_{\eta_0^{st}}$	-	0.9966 (0.9961, 0.9972)	0.9969 (0.9963, 0.9975)
$\sigma_{\eta_0^{st}}^2$	-	140.37 (130.31, 150.30)	86.81 (79.14, 94.11)
$\rho_{\eta_{TCC}^s}$	-	-	0.9999 (0.9995, 1.0000)
$\sigma_{\eta_{TCC}^s}^2$	-	-	34.71 (28.55, 41.29)
σ_ϵ^2	0.70 (0.61, 0.79)	0.59 (0.54, 0.66)	0.56 (0.51, 0.63)
$\widehat{\text{elpd}}_{\text{WAIC}}$	-113123.6	-112481.2	-112496.2
$\widehat{p}_{\text{WAIC}}$	7078.1	6622.7	6461.9
WAIC	226247.3	224962.4	224992.4
$\widehat{\text{elpd}}_{\text{diff}}$	-642.5 (51.9)	0 (0)	-15.0 (22.2)

Table 1: Parameter estimates for candidate models fit to FIA data. Estimates are posterior medians with 95% credible intervals given in parentheses. Estimates for WAIC and associated statistics are given in the last several rows. The last row holds the estimated $\widehat{\text{elpd}}_{\text{WAIC}}$ difference with the “best” fitting Submodel 1 and associated standard error $\widehat{\tau}_{\text{diff}}$ in parentheses.

variation in forest carbon density. The Full model’s SVC $\beta_{TCC} + \boldsymbol{\eta}_{TCC}^s$, shown in Figure 3, is particularly useful for identifying x_{TCC} ’s nonstationary impact on carbon density, whereby an increment change in x_{TCC} in northern California, the Pacific Northwest, the southern Appalachian Mountains, and southern New England (i.e., the brighter color regions) is associated with a greater change in carbon density than regions with darker colors. For example, per unit area, a county with 50% forest canopy cover in the Pacific Northwest, Appalachian Mountains, or New England will have more carbon than a county with 50% forest canopy cover in the midwest, Texas, or southern Florida.

Given the clear nonstationarity seen in Figure 3, all subsequent results presented are based on the Full model. Figures S17 and S18 map $\mu_{j,t}$ ’s posterior distribution mean and standard deviation, respectively. For counties that have complete missingness (i.e., no direct estimates in the study period), as depicted in Figure S15, estimates come from the posterior predictive distribution of $\mu_{j,t}$ and will typically have a greater uncertainty than those borrowing information from the given county’s direct estimates. This greater uncertainty is most apparent in central and some north-central counties when comparing Figures S18 and S15. If increasing sample size is not an option, then reducing σ_ϵ^2 , via additional predictor variables or random effects, will reduce the posterior predictive distribution’s dispersion.

Carbon density trend estimates for θ_j are shown in Figure 4(a). Figure 4(b) shows only

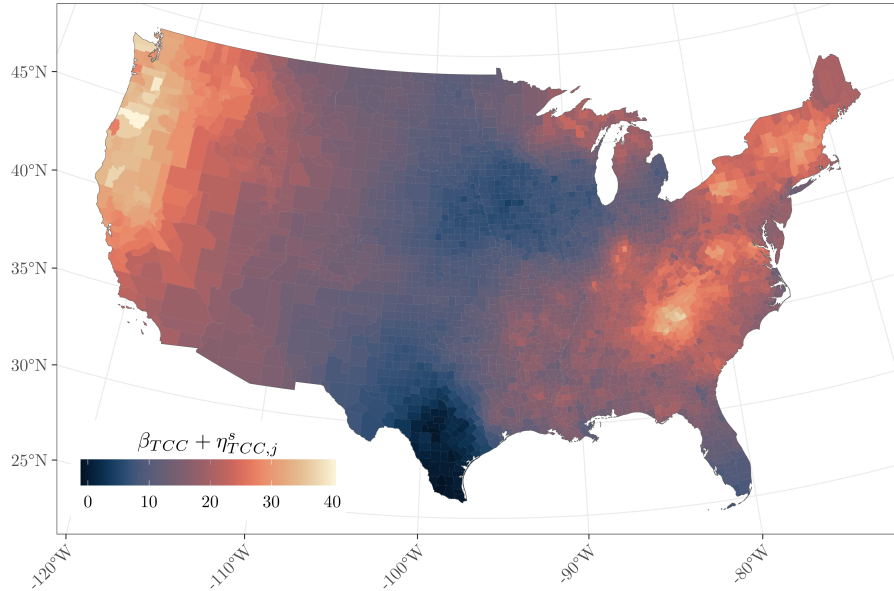


Figure 3: Posterior median of the Full model’s space-varying coefficient $\beta_{TCC} + \eta_{TCC,j}^s$ fit to the FIA data.

those county values in Figure 4(a) that have a posterior distribution 95% credible interval that does not include zero. Here, several expected patterns in carbon density increase and decrease emerge. As detailed in Harris et al. (2016), Hoover and Smith (2021), and similar studies on forest biomass/carbon change in the CONUS, factors including fire, insect, disease, harvest, and changing forest age and land use drive the observed patterns of carbon loss in western counties and the Ohio Valley. In contrast, the increase in carbon density in the southeast and Maine is primarily due to increases in industrial forest operations, changes in forest age and structure, and increased forest productivity (Hoover and Smith, 2021; Hogan et al., 2024).

Figure 5 shows the direct and model estimates for $\mu_{j,t}$ for the two counties with the largest negative and positive θ_j estimates in Figure 4(b). A list of counties with the 10 largest negative and positive θ_j estimates in Figure 4(b) are given in Table S4. As recorded in Table S4, Lake, California has the largest negative θ_j estimate among all counties in the CONUS. Over the study period, Lake County’s estimate for θ_j was -1.25 (-1.62, -0.88) (Mg/ha/year). This negative trend is evident in Lake County’s $\mu_{j,t}$ estimates shown in Figure 5(a). Much of Lake County’s carbon loss occurred in 2018 as a result of the River, Ranch, and Pawnee Fires that burned an estimated 48,400 (ha) (Tyukavina et al., 2022). The effect of these 2018 fires is clearly seen in the model estimates and TCC values in Figure 5(a). Given the relatively small sample sizes, it is not surprising that direct estimates do not capture the impact of fire on forest carbon. With lack of direct estimate information, the model learns from TCC, which clearly shows a loss of canopy cover starting in 2018

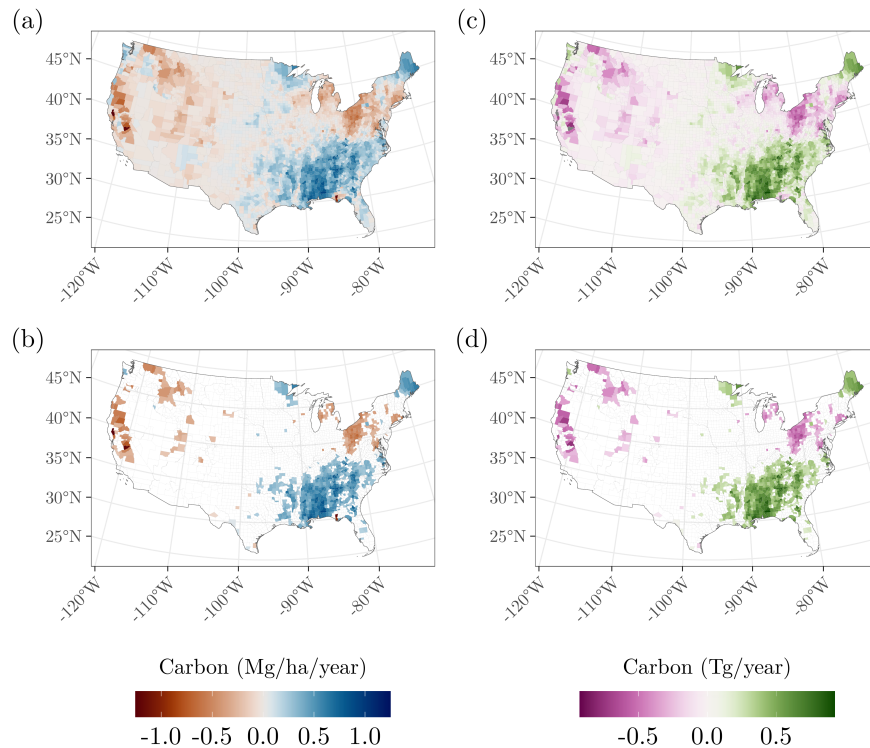


Figure 4: Estimates from the Full model. (a) Estimated linear trend in forest carbon density θ_j (Mg/ha/year). Values are each county’s posterior distribution median. (b) Counties from (a) that have posterior distribution 95% credible intervals that exclude zero. (c) Estimated linear trend in forest carbon total $A_j\theta_j$ (Tg/year), where A_j is the j^{th} county’s area in hectares. (d) Counties from (c) that have posterior distribution 95% credible intervals that exclude zero. The 10 counties with the largest and smallest values in (b) and (d) are given in Tables S4 and S5, respectively.

(Figure 5(a)). Escambia Alabama has the largest positive θ_j estimate among all counties in the CONUS. Over the study period, Escambia County’s estimate for θ_j was 0.92 (0.67, 1.20) (Mg/ha/year). This positive trend is seen in Figure 5(b) and reflects carbon accumulation in the county’s intensively managed softwood plantations. Figures comparable to Figure 5 for all counties are provided in Supporting Information Section S6.1.

Given the county area and our estimate for carbon density, an estimate of total carbon trend is $A_j\theta_j$, where A_j is the area of the j^{th} county in hectares. These total county carbon estimates are shown in Figures 4(c,d), with the 10 largest negative and positive county estimates given in Table S5. This table shows that, once scaled by county area, large-area counties in California and Maine dominate negative and positive carbon trends, respectively. Moreover, we observe clear regional patterns, with the most negative carbon trends occurring in the west and the most positive in the northeast and southeast.

Following the simulated data analysis, we calculated estimates for Δ_j and $A_j\Delta_j$ to investigate carbon change over the study period. These change patterns were similar to those for θ_j and are presented in Figure S19.

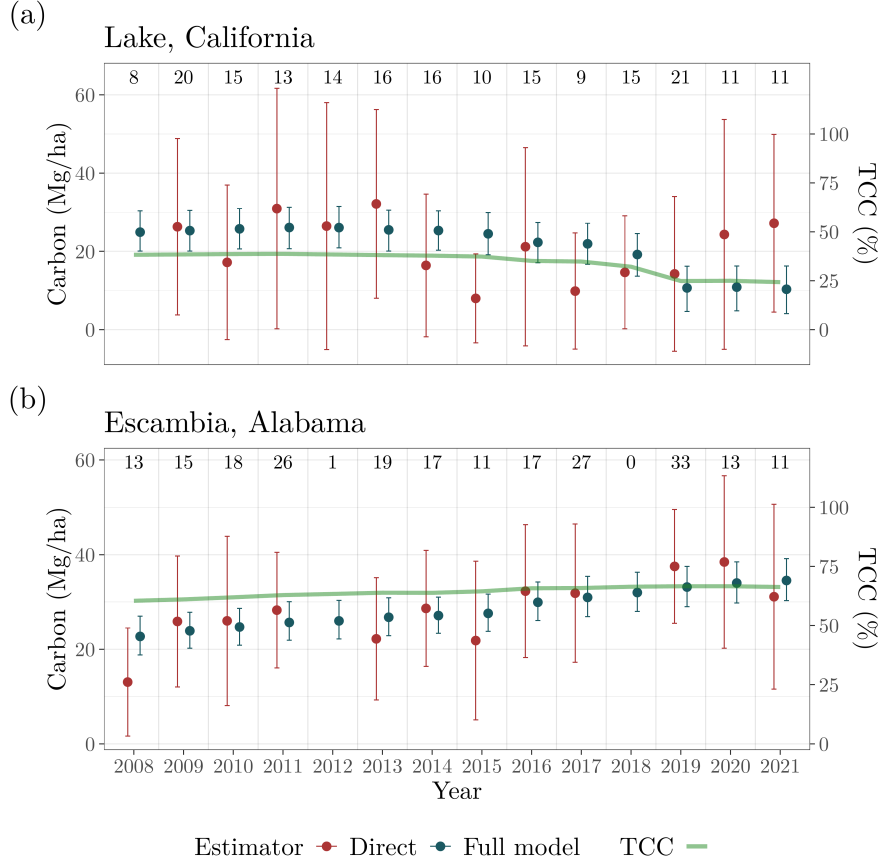


Figure 5: Direct and model estimates for $\mu_{j,t}$ along with TCC values for counties with the largest negative and positive θ_j estimates given in Table S4. Sample size $n_{j,t}$ for each county and year is given across the top of each subpanel. Estimate means and medians are shown as points with 95% confidence and credible interval bars for direct and model estimates, respectively. When $n_{j,t} \leq 2$ or all observations are zero, the direct estimate is not available, e.g., Escambia, Alabama in 2012 and Lake, California in 2008, respectively.

For administrative and reporting purposes, FIA partitions the CONUS into four regions shown in Figure S21: Northern; Pacific Northwest; Rocky Mountain; Southern. Following (15), regional annual total carbon estimates for $\Omega_{\mathcal{J}}$ are given in Figure 6. This figure highlights the strong regional trends seen in Figures 4 and S19. Tabular estimates for trend $A_{\mathcal{J}}\theta_{\mathcal{J}}$ (Tg/year) and change $A_{\mathcal{J}}\Delta_{\mathcal{J}}$ (Tg) by FIA region are given in Table S6 and again underscores patterns seen in Figure 6. Specifically, over the 14 year period, we see no significant change in carbon in the Northern region, significant carbon loss in the Pacific Northwest and Rocky Mountain regions, and significant carbon gain in the Southern region.

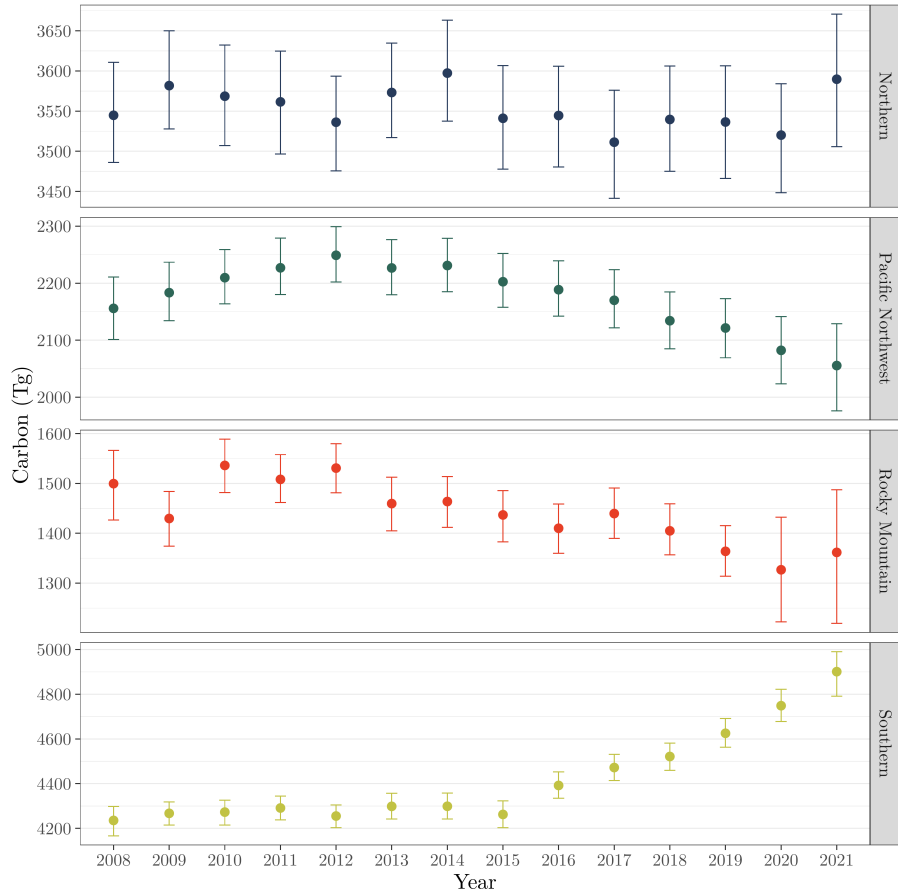


Figure 6: Full model estimates for annual carbon $\Omega_{\mathcal{J},t}$ within FIA regions shown in Figure S21. Point and bars are the median and 95% credible interval for posterior distributions summarized over region and year following (15).

4 Discussion and summary

The simulation study and FIA data analysis demonstrate the proposed model’s usefulness for delivering estimates for spatial and temporal extents with limited observations. The SAE model is assembled using components that are well documented in the statistical literature. In the current setting, the FH model provides a mechanism to learn from direct estimates, predictor variables, and spatially and temporally structured random effects. Casting this model into a Bayesian estimation framework provides additional opportunities to glean information from the data and survey design. For example, our proposed informative IG prior on $\sigma_{j,t}^2$ is an intuitive way to obtain potential information from the observed sample size $n_{j,t}$. The Bayesian framework also provides easy access to posterior distributions derived from the latent mean, e.g., total, trend, and change, for both individual areal units and aggregates of areal units. Further, inference from areal units with no observations is available via the latent mean’s posterior predictive distribution, which allows us to make spatially and temporally complete estimates (e.g., for every county and year in the CONUS). This ability to use auxiliary information to adjust/inform direct estimates seems particularly useful for meeting evolving inferential demands placed on existing NFI programs.

As always, there is “no free lunch.” SAE models, including the one highlighted here, simply adjust or smooth the direct estimate. If there are issues with the direct estimate, then those issues persist in the model estimate. For example, the simulation study showed that those counties with small sample sizes had biased direct estimates and those biases might persist in the model estimates. However, if the adjacent areal units and/or times had more reliable data or larger sample sizes, then the structured random effects shrink the mean toward the average of the proximate neighbors, which could mitigate bias. In fact, one reason why CAR random effects are popular in SAE is because of this bias reduction in sparsely populated regions. The simulation study identified clear advantages to using the model, including improved accuracy and uncertainty quantification in most cases.

Several properties and limitations of area-level FH models require further consideration. First, if all observations within an areal unit have the same value, there will be no direct estimate variance and, hence, that information is not available to train the model. Therefore, it is treated as missing although it provides valuable information. In our study, this occurred when all plots within a county and year had zero carbon and, in such cases, we relied on the TCC predictor and random effects to inform the posterior predictive distribution from which we draw inference. Second, the FH model is most often applied to continuous and Normally distributed variables, although there are transformations that might accommodate discrete count-like variables, see, e.g., Ghosh et al. (2022). There are many forest variables that do not have Normal support or lend themselves well to transformation, and in such cases the FH model will not be suitable. Lastly, area-level models, as presented here, do not support prediction for units not included in the initial adjacency matrix. If inference for a new areal unit is needed, the unit must be added to the adjacency matrix and the model refit. If any of these limitations are prohibitive and NFI plot measurements are indexed in space and time, then one might consider unit-level models based upon point-referenced geostatistical models.

NFIs provide critical information on the ecological health and economic viability of forests. NFI programs will continue to be asked for finer spatial and temporal resolution

information on forest parameter status, trend, and change to support initiatives like forest carbon monitoring required by the UNFCCC. Financial circumstances limit most NFI programs’ ability to collect sufficient data to meet these user needs, especially when estimates are provided by classical design-based methods. SAE models, like those proposed here, are needed to help bridge this gap and allow NFIs to provide high-quality and reliable estimates for key forest parameters.

Supporting information

S5 Simulation study

We follow a frequentist view for the simulation study, where a single population is generated using fixed and known values for parameters, then estimates for parameters are computed from each of a large number of independent samples, i.e., R replicates, taken from the population. These estimates are then compared with population parameters using a set of measures that assess the estimators’ bias, accuracy, and precision. Specifically, we are interested in assessing estimator quality for $\mu_{j,t}$ and derived parameters θ_j and Δ_j . The four estimators considered are the direct (1), Full model (8), Submodel 1 (9), and Submodel 2 (10).

S5.1 Simulated population and replicate samples

To mimic qualities of the observed annual county-level data, we simulated a population comprising 7,809,952 point-referenced population units laid out in a 1-by-1 (km) regular grid over the CONUS land area. Each point-referenced population unit represents a possible sampling unit (i.e., FIA plot). At each population unit, we simulated a spatially and temporally correlated outcome value with dependence structure similar to the observed FIA plot carbon density (Mg/ha) data. Specifically, the outcome $y_t(\boldsymbol{\ell})$ at generic population unit location $\boldsymbol{\ell}$ and time t is given by

$$\begin{aligned} y_t(\boldsymbol{\ell}) &= \zeta_0 + u_t(\boldsymbol{\ell}) + \zeta_1 v_{TCC,t}(\boldsymbol{\ell}) + \epsilon_t(\boldsymbol{\ell}), \quad \epsilon_t(\boldsymbol{\ell}) \stackrel{iid}{\sim} N(0, \sigma_y^2), \\ u_t(\boldsymbol{\ell}) &= u_{t-1}(\boldsymbol{\ell}) + w_t(\boldsymbol{\ell}), \quad w_t(\boldsymbol{\ell}) \stackrel{ind}{\sim} GP(0, C(\cdot, \gamma)), \quad t = 1, 2, \dots, T, \end{aligned} \quad (\text{S19})$$

where ζ_0 and ζ_1 are an intercept and slope coefficient, $u_t(\boldsymbol{\ell})$ is a space-time varying intercept, and $\epsilon_t(\boldsymbol{\ell})$ is a serially and spatially uncorrelated residual term following a mean zero Normal distribution with variance σ_y^2 . The temporally independent $w_t(\boldsymbol{\ell})$ follows a mean zero GP with exponential covariance function $C(\cdot, \gamma) = \sigma_w^2 \exp(-\gamma \|\boldsymbol{\ell} - \boldsymbol{\ell}'\|)$, where σ_w^2 is the spatial variance, $\|\boldsymbol{\ell} - \boldsymbol{\ell}'\|$ is the Euclidean distance between two, possibly different, locations, and γ is the decay parameter that controls the correlation. We set $u_0(\boldsymbol{\ell}) = 0$.

To generate outcome patterns and relationships similar to the real FIA data, values for $v_{TCC,t}(\boldsymbol{\ell})$ were taken from the spatially and temporally coinciding TCC pixels and parameter values were set to $\zeta_0 = 1.5$, $\zeta_1 = 2$, $\sigma_y^2 = 1,000$, $\sigma^2 = 10$, and $\gamma = 0.003$. These parameter values were chosen through exploratory regression analysis. The spatial decay parameter value produces a high correlation between adjacent counties (as seen in the real FIA data

when aggregated to the county and year level). Also, to mimic observed forest and non-forest patterns, $y_t(\ell)$ was set to zero when $v_{TCC,t}(\ell) = 0$ and when the simulated $y_t(\ell)$ was less than zero.

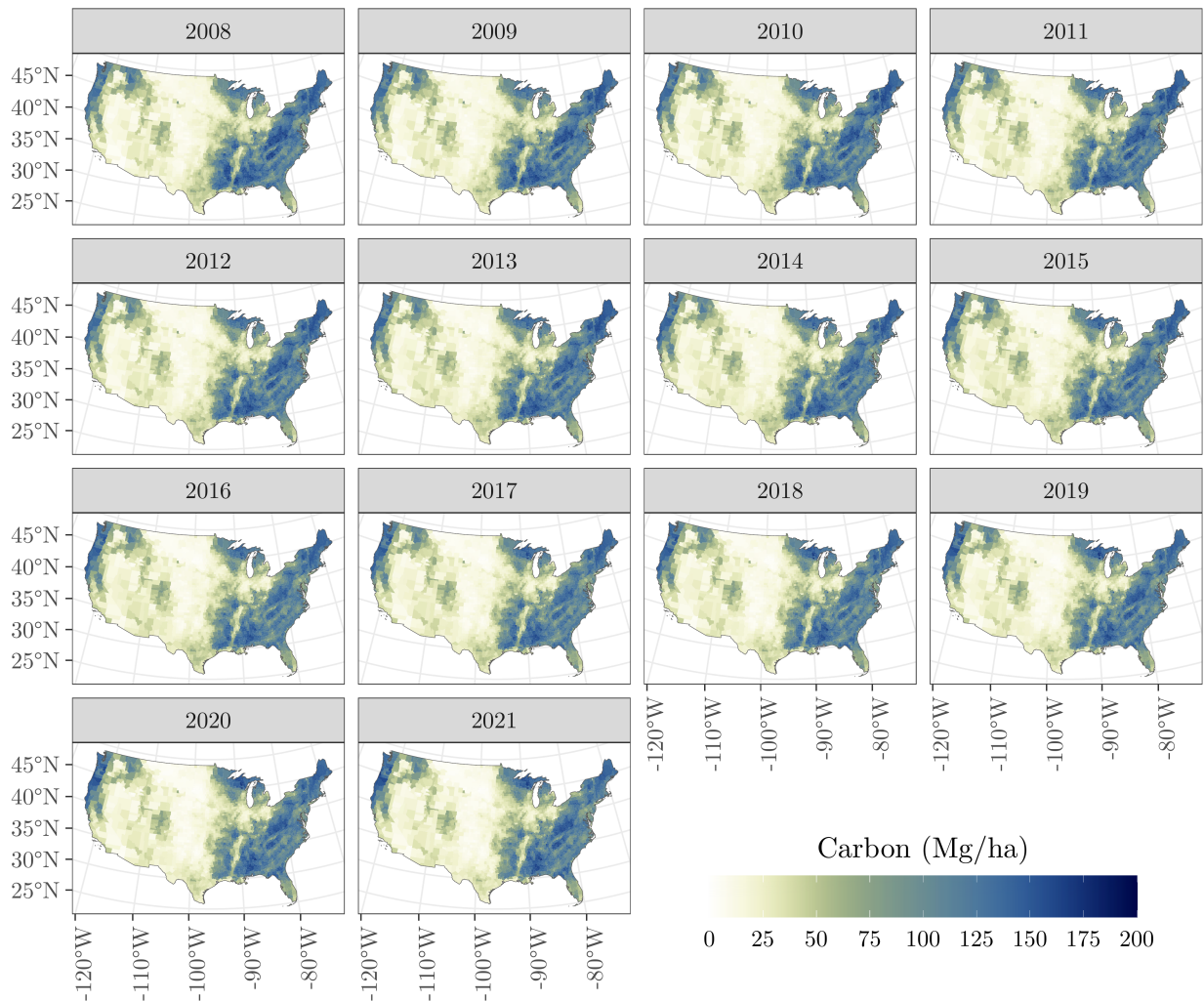


Figure S7: Simulated population forest carbon density $\mu_{\text{true},t,j}$ (Mg/ha).

Simulated population values from (S19) were averaged within each county and year and serve as the “true” mean $\mu_{\text{true},j,t}$ shown in Figure S7. This true mean was used to calculate $\theta_{\text{true},j}$ using (12) between 2008 and 2021 and $\Delta_{\text{true},j}$ using (14) with $t_1 = 2008$ and $t_2 = 2021$. The resulting true county-level trend and change are shown in Figures S8(a) and S9(a), respectively.

Following (1) and (2), annual county-level direct estimates were generated from each of $R=100$ sample replicates. Each replicate comprises a simple random sample from the population, with the sample size for each county and year set to that of the FIA data (Figure 1). Although the proposed models can accommodate sample sizes of zero (as demonstrated in the FIA data analysis Section 3.3), comparisons consider only those counties with two or

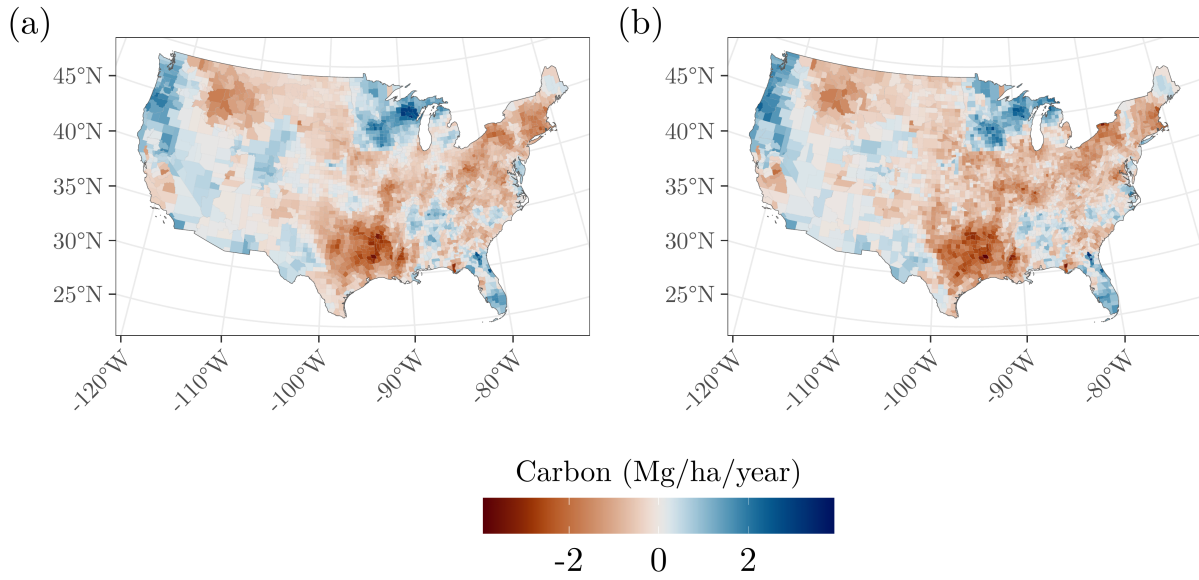


Figure S8: (a) Simulated population linear slope trend in forest carbon density θ_j (Mg/ha/year). (b) Full model estimates for θ_j using the first replicate's sample data.

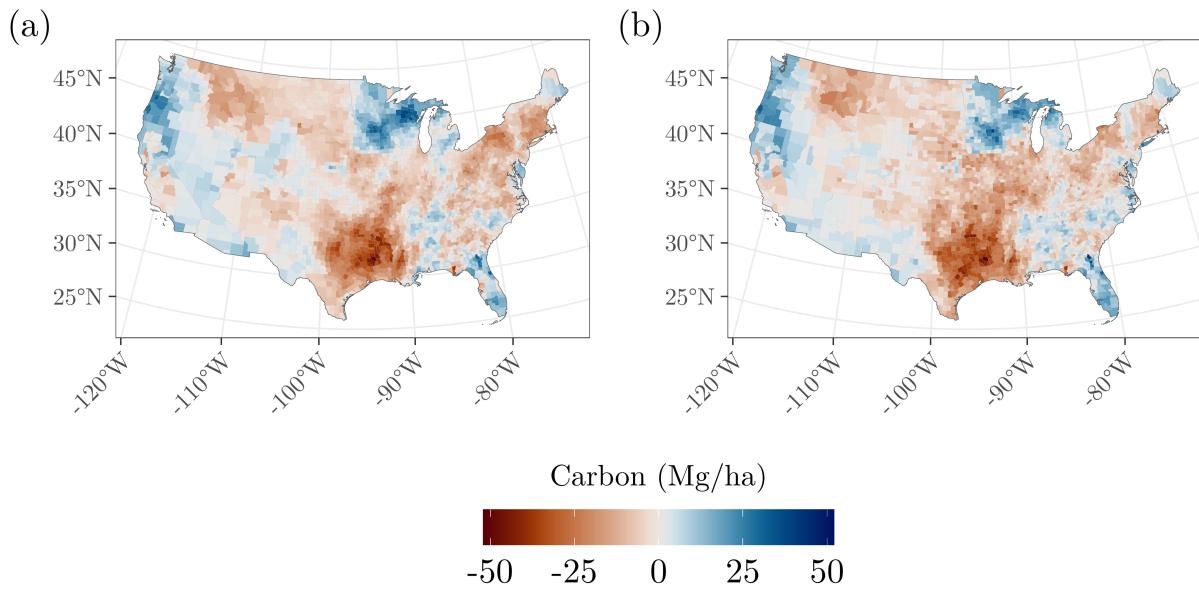


Figure S9: (a) Simulated population change in forest carbon density Δ_j (Mg/ha) between $t_1=2008$ and $t_2=2021$. (b) Full model estimates for Δ_j using the first replicate's sample data.

more plots so that the direct estimator's uncertainty quantification can be compared with the models'.

S5.2 Comparison among estimators

Given $\mu_{\text{true},j,t}$ and R estimates from each estimator, we consider measures of bias, root mean squared error (RMSE), empirical confidence and credible interval coverage rates, and width between the lower and upper 95% confidence and credible interval bounds, as defined below.

Systematic difference between estimate and truth is evaluated using

$$\text{Bias}_{j,t,l} = \frac{\sum_{r=1}^R (\mu_{j,t,l,r} - \mu_{\text{true},j,t})}{R}, \quad (\text{S20})$$

where $\mu_{j,t,l,r}$ is the l^{th} estimator's point estimate given sample data from the r^{th} replicate. The point estimate for the candidate models is the posterior mean of $\mu_{j,t}$ and $\hat{\mu}_{j,t}$ for the design-based estimator.

Average accuracy is evaluated using

$$\text{RMSE}_{j,t,l} = \sqrt{\frac{\sum_{r=1}^R (\mu_{j,t,l,r} - \mu_{\text{true},j,t})^2}{R}}. \quad (\text{S21})$$

Average empirical coverage rate is evaluated using

$$\text{Cover}_{j,t,l} = \frac{\sum_{r=1}^R I(\mu_{j,t,l,r}^L \leq \mu_{\text{true},j,t} \leq \mu_{j,t,l,r}^U)}{R}, \quad (\text{S22})$$

where $I(\cdot)$ is an indicator function, and $\mu_{j,t,l,r}^L$ and $\mu_{j,t,l,r}^U$ are the lower and upper uncertainty quantification bounds. Here we consider the 95% credible interval bounds for the candidate models and 95% confidence intervals for the design-based estimator.

Average precision is evaluated using

$$\text{Width}_{j,t,l} = \frac{\sum_{r=1}^R (\mu_{j,t,l,r}^U - \mu_{j,t,l,r}^L)}{R}. \quad (\text{S23})$$

These performance measures are summarized in Figure S10, where each point is a county and year combination (i.e., there are N points in each figure sub-panel). County and year combinations are ordered along the x -axis by increasing sample size.

Figure S10(a) shows all estimators can be biased when sample size is small, e.g., $n_{j,t} \lesssim 50$, and this bias can increase as sample size decreases. For some of the smallest sample sizes, e.g., $n_{j,t} = 2$, the direct estimate for a given county and year can produce bias as large as approximately ± 10 (Mg/ha). The models can yield slightly greater bias for small sample sizes, with Submodel 2 exhibiting the largest bias among the estimators.

Figure S10(b) shows the direct estimator has larger RMSE (poorer accuracy) relative to the models when $n_{j,t} \lesssim 100$ and particularly so when $n_{j,t} \lesssim 25$. Figure S10(c) shows the direct estimator achieves close to the expected 95% confidence interval coverage rate even for small samples. In contrast, the models demonstrate dramatically lower than expected credible interval coverage rates when the sample size is small. As shown in Figure S10(d), the direct estimator's confidence interval coverage rate of $\sim 95\%$ reflects its extremely large confidence interval widths. Conversely, the models' relatively poor credible interval coverage rates are due to overly narrow credible intervals.

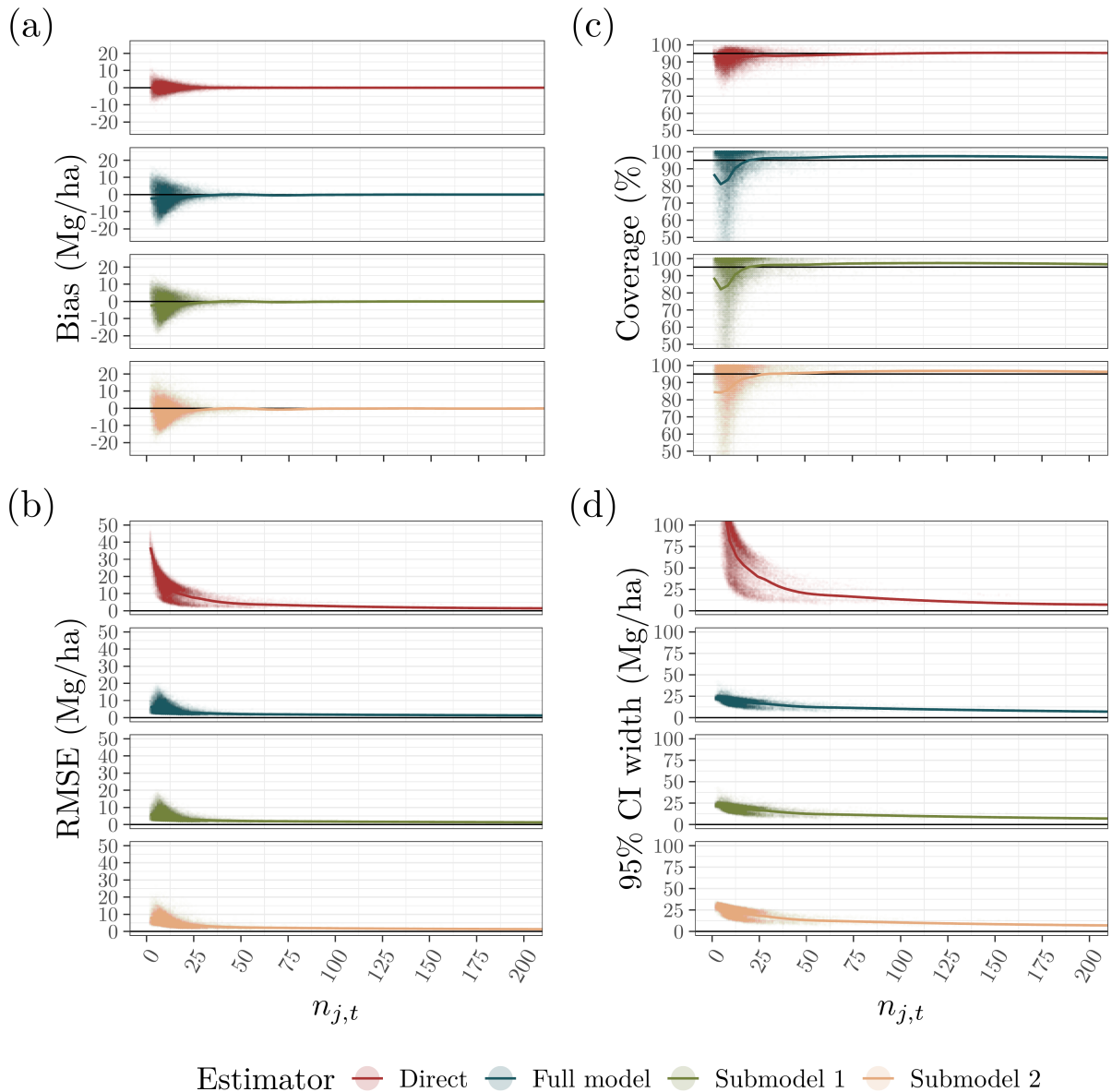


Figure S10: Performance of estimators for $\mu_{j,t}$ from the simulation analysis. Each point value represents the average over R replicates for a county and year. A loess line is added to indicate point scatter trend across sample size ($n_{j,t}$).

Figure S11 shows estimates for three counties based on the first replicate's sample data, provides some insight into the summaries given in Figure S10, and demonstrates how estimates compare for low, moderate, and moderately large sample sizes (figures for all J counties are provided in the Supplemental Material). Estimates for San Francisco, CA, are given in Figure S11(a). For small, urban counties like San Francisco that have low forest carbon density values, little information is provided by direct estimates due to small sample sizes, and model estimates are informed by the TCC predictor variable and direct estimates

in adjacent years and counties. In these cases, our results routinely show the models provide accurate estimates, but their credible intervals are often too narrow (i.e., do not cover the true value at the expected rate). This trend is captured in Figures S10(b-d). In contrast, model estimates for counties with moderately large sample sizes, such as Sullivan, PA, Figure S11(b), and larger samples sizes, such as Hancock, ME, Figure S11(c), have improved accuracy and precision over direct estimates.

The simulated population values for the trend θ_j (12) and change Δ_j (14) parameters are shown in Figures S8 and S9, respectively. For these parameters, the models are able to deliver improved accuracy and precision with bias comparable to the direct estimator and coverage rate closer to the expected 95%, see Figures S12 and S13, respectively. To visualize this accuracy spatially, the parameters’ true values shown in Figures S8(a) and S9(a) can be compared with estimates based on the first replicate’s sample data given in Figures S8(b) and S9(b).

Returning to Figure S10, we observe clear differences between the direct and model estimators; however, it is difficult to discern performance differences between the models. Following Section 2.4, WAIC was estimated for each candidate model and each replicate. When comparing WAIC scores, Submodel 1 and the Full model estimates are comparable, and both are substantially better than Submodel 2 (Table S2). As specified in (9), Submodel 1 has a space- and time-varying intercept but a spatially and temporally invariant regression coefficient; hence, Submodel 1 is consistent with the data simulation model (S19). We therefore might expect Submodel 1 to outperform the Full model. However, given the flexibility of the Full model, it is not surprising that the information criterion does not show a substantial difference between Submodel 1 and the Full model. Similar results presented in Doser et al. (2024) showed that WAIC could not differentiate between a space-varying intercept and a SVC model when simulated data came from a space-varying intercept model.

Parameter	Candidate models		
	Submodel 2	Submodel 1	Full model
$\widehat{\text{elpd}}_{\text{WAIC}}$	-164857.2 (157.0)	-164177.9 (156.2)	-164164.1 (155.3)
$\widehat{p}_{\text{WAIC}}$	9630.5 (96.8)	8477.8 (104.9)	8454.4 (103.7)
WAIC	329714.3 (313.9)	328355.7 (312.3)	328328.1 (310.7)

Table S2: Simulated data estimates for WAIC and associated statistics. Values are the average over the replicates with the standard deviation given in parentheses.

Table S3 provides parameter estimates for each candidate model based on the first replicate’s sample data, which are representative of those generated from the other $R - 1$ sample datasets. Although not of direct interest to model comparison, these estimates give a sense of the process parameter values and, in particular, the strength of the spatial and temporal correlation parameters. The strong spatial and temporal correlations seen in the Submodel 1 and Full model intercept random effect are also observed in the FIA data analysis presented in Section 3.3. Given the similarities between the simulated and FIA data, we gain some assurance that the estimators’ qualities explored in Figures S10, S12, and S13 are transferable

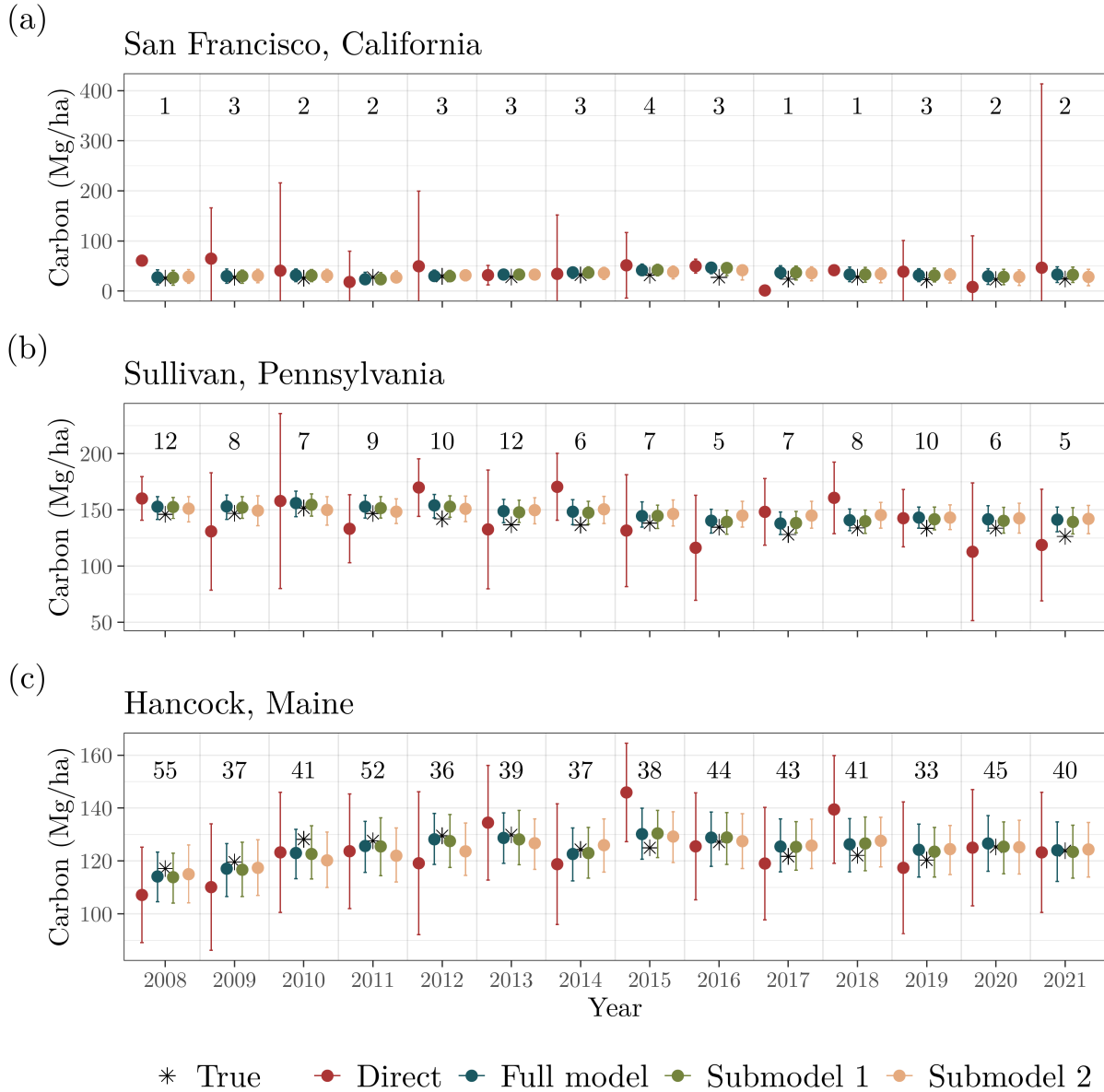


Figure S11: Simulated $\mu_{true,j,t}$ values and estimates based on sample data from the first replicate. Sample size $n_{j,t}$ for each county and year is given across the top of each subpanel. Estimate means and medians are shown as points with 95% confidence and credible interval bars for direct and model estimates, respectively. When the sample size is one, confidence intervals are not available for the direct estimate.

to the FIA data analysis.

By design, the hierarchical prior for $\sigma_{j,t}^2$ given in (2.2) provides a varied effect on its posterior distribution. This effect is directly related to the number of observations ($n_{j,t}$) used to calculate the associated direct estimate, whereby more weight is placed on the prior mean as $n_{j,t}$ increases. As shown in Figure S14(a), for $n_{j,t} \gtrsim 8$, the posterior mean more

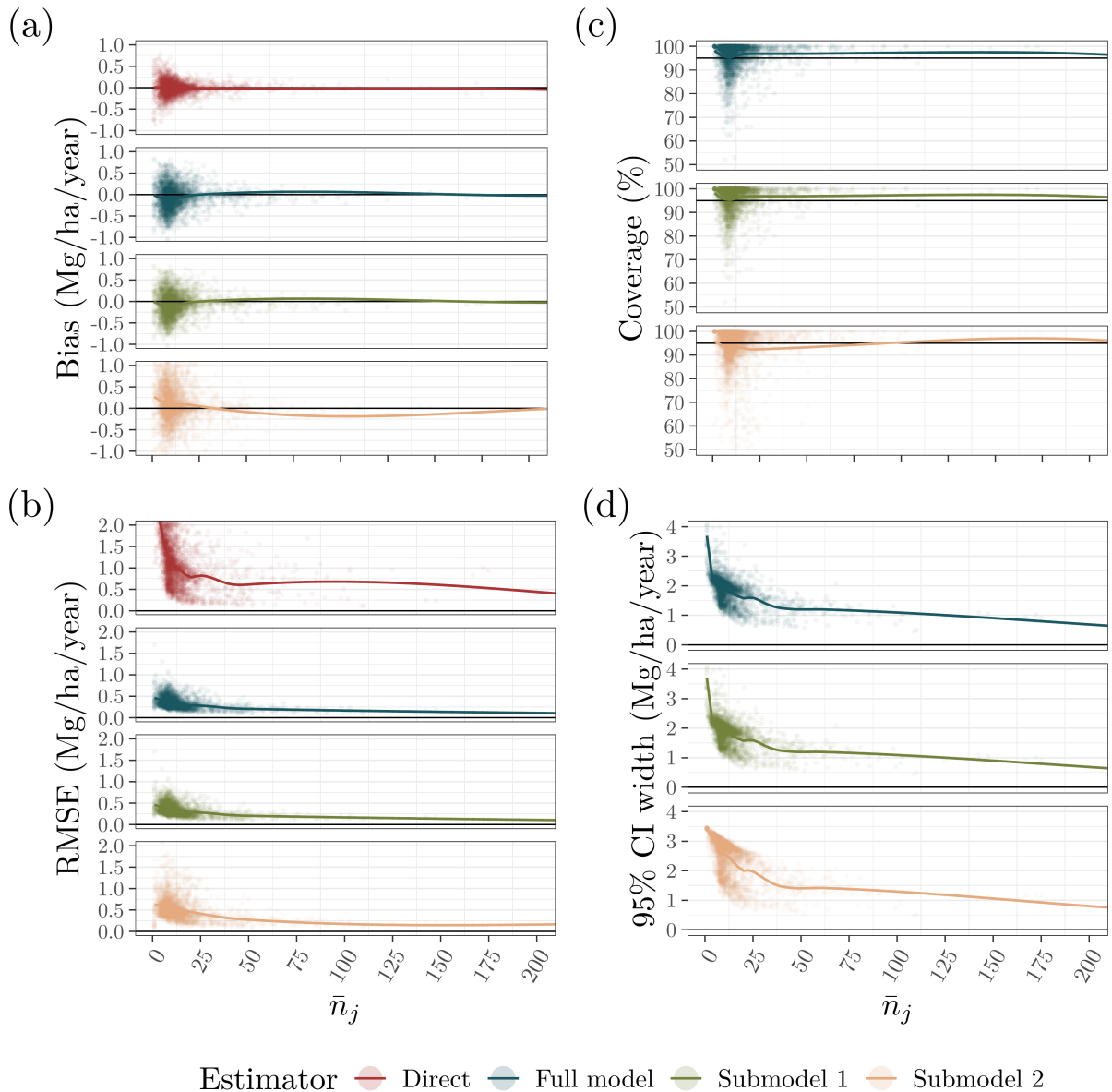


Figure S12: Simulation analysis estimator performance for θ_j . Point values are the average over R replicates for a county. A loess line is added to indicate point scatter trend across average sample size values ($\bar{n}_j = \frac{1}{T} \sum_{t=1}^T n_{j,t}$).

closely reflects the prior mean, (blue points along the 1:1 line) while discrepancy between prior and posterior means is clear for $n_{j,t} \lesssim 4$ (yellow to red points away from the 1:1 line). This discrepancy stems from learning that occurs from other information present in the data that the model essentially weights more heavily, including neighboring direct estimates, predictor variables, and structured random effects. This balance between information sources conditional on $n_{j,t}$ is also seen in Figure S14(b), where we compare $\mu_{j,t}$'s direct estimate to its estimated posterior distribution mean. Here, again, as $n_{j,t}$ increases, more information is

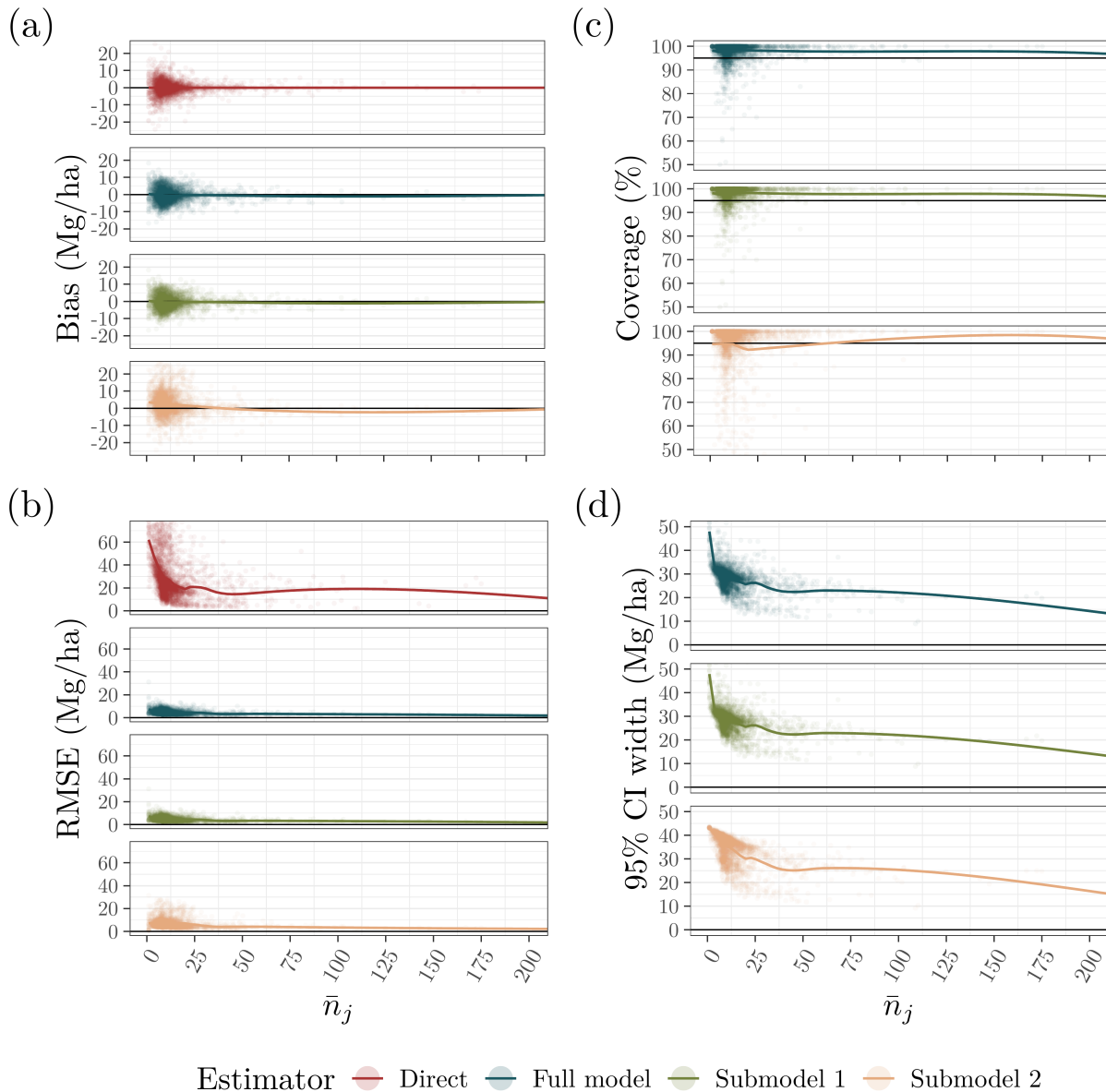


Figure S13: Simulation analysis estimator performance for Δ_j . Each point value represents the average over R replicates for a county. A loess line is added to indicate point scatter trend across average sample size values ($\bar{n}_j = \frac{1}{T} \sum_{t=1}^T n_{j,t}$).

drawn from the direct estimate (blue points close the 1:1 line), and when $n_{j,t}$ is small, more information is drawn from other sources and estimates can be quite different from the direct estimate (red points away from the 1:1 line).

S6 Supporting figures and tables

Parameter	Candidate models		
	Submodel 2	Submodel 1	Full model
β_0	69.34 (69.03, 69.73)	68.43 (67.79, 70.55)	66.65 (65.72, 67.27)
β_{TCC}	46.66 (46.42, 46.92)	48.33 (47.94, 48.82)	47.65 (46.17, 48.90)
$\alpha_{\eta_0^t}$	0.9192 (0.9119, 0.9265)	-	-
$\sigma_{\eta_0^t}^2$	82.79 (77.88, 87.10)	-	-
$\rho_{\eta_0^{st}}$	-	0.9984 (0.9979, 0.9989)	0.9989 (0.9982, 0.9993)
$\alpha_{\eta_0^{st}}$	-	0.8918 (0.8811, 0.9053)	0.8773 (0.8645, 0.8893)
$\sigma_{\eta_0^{st}}^2$	-	111.74 (103.21, 121.31)	99.13 90.36 109.08
$\rho_{\eta_{TCC}^s}$	-	-	0.9998 (0.9986, 1.00)
$\sigma_{\eta_{TCC}^s}^2$	-	-	9.75 (7.47, 13.17)
σ_{ϵ}^2	7.06 (5.82, 8.51)	9.66 (8.56, 10.94)	10.07 (8.83, 11.37)

Table S3: Simulated data analysis parameter estimates for candidate models using first replicate's sample data. Estimates are posterior medians with 95% credible interval given in parentheses.

Decreasing			Increasing		
State	County	Carbon	State	County	Carbon
California	Lake	-1.25 (-1.62, -0.88)	Alabama	Escambia	0.92 (0.67, 1.20)
Florida	Calhoun	-1.21 (-1.63, -0.76)	Georgia	Cobb	0.87 (0.58, 1.17)
California	Mariposa	-1.19 (-1.57, -0.77)	Tennessee	Rhea	0.86 (0.59, 1.15)
Florida	Gulf	-0.94 (-1.40, -0.52)	Mississippi	Hancock	0.85 (0.55, 1.14)
California	Tuolumne	-0.76 (-1.04, -0.48)	Alabama	Dallas	0.83 (0.58, 1.07)
California	Shasta	-0.71 (-0.98, -0.44)	Mississippi	Harrison	0.82 (0.52, 1.10)
Pennsylvania	Allegheny	-0.67 (-0.92, -0.42)	Alabama	Conecuh	0.82 (0.54, 1.10)
California	Napa	-0.66 (-1.00, -0.34)	Alabama	Greene	0.81 (0.54, 1.07)
Virginia	Falls Church	-0.64 (-1.11, -0.21)	Mississippi	Stone	0.81 (0.55, 1.08)
Ohio	Carroll	-0.63 (-0.93, -0.34)	Georgia	Polk	0.80 (0.55, 1.07)

Table S4: Ten largest decreasing and increasing estimates for carbon density trend θ_j (Mg/ha/year) from 2008 to 2021 across the CONUS. Estimates are posterior medians with 95% credible interval values given in parentheses.

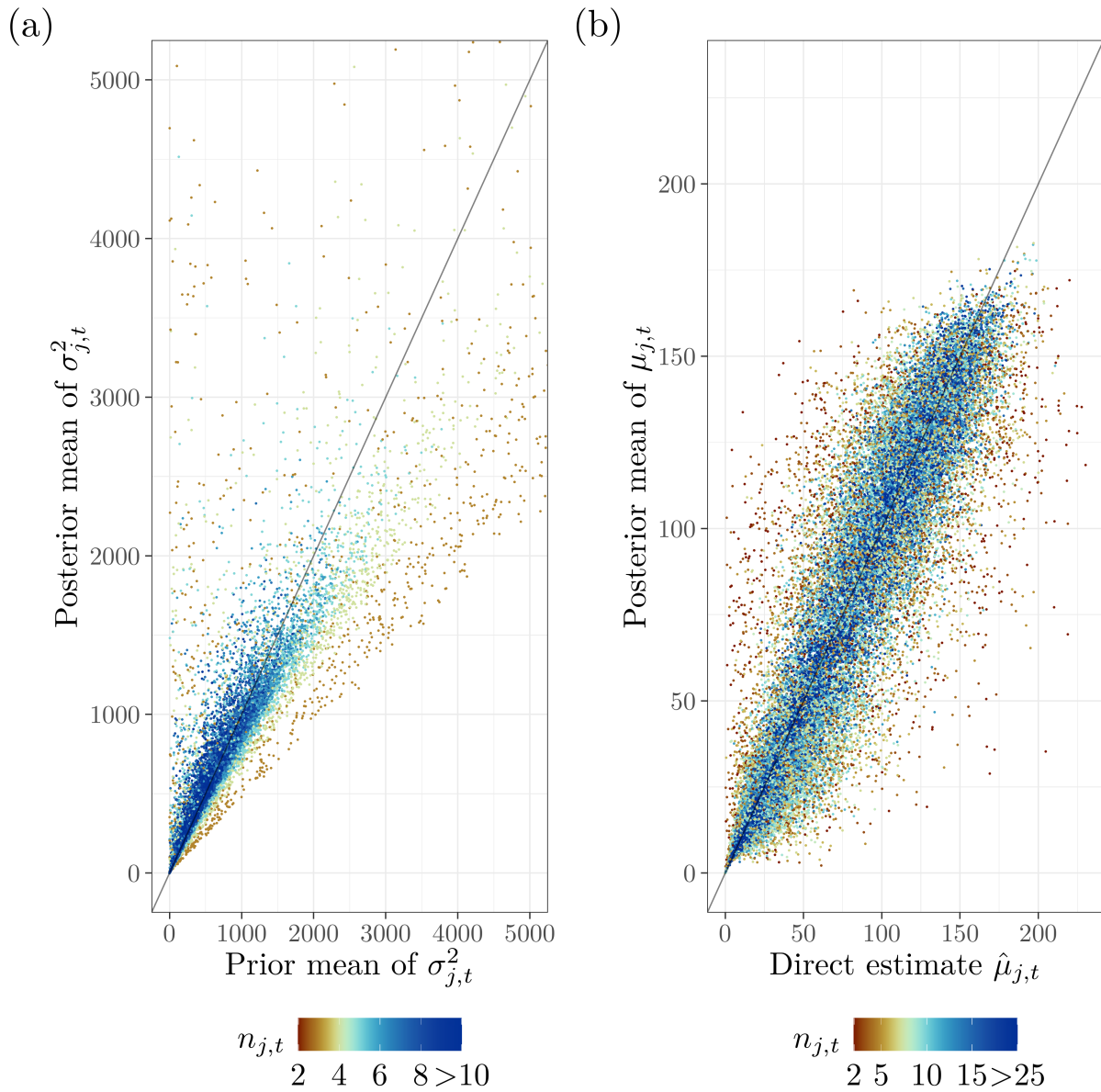


Figure S14: Full model parameter estimates using first replicate's sample data. (a) $\sigma_{j,t}^2$ prior mean versus its posterior mean. (b) $\mu_{j,t}$ direct estimate versus its posterior mean. Points colored by sample size.

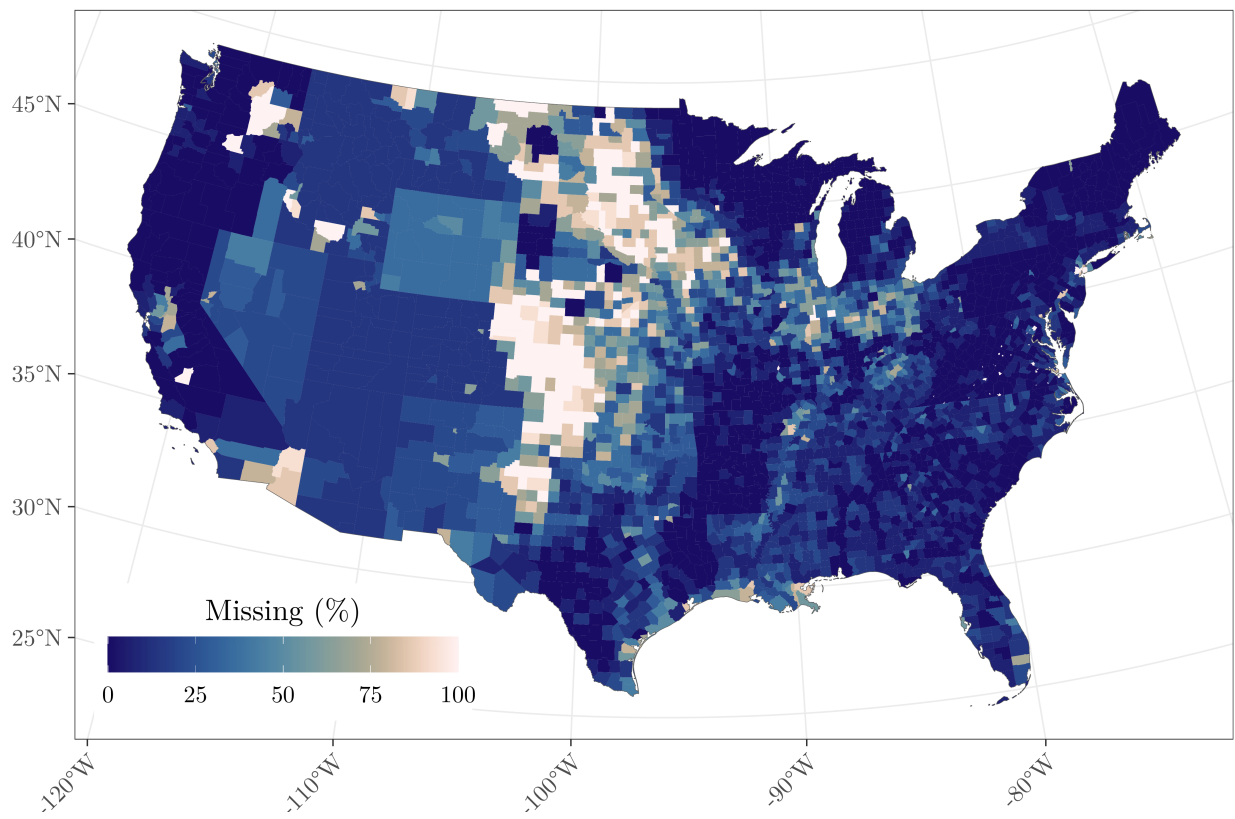


Figure S15: Percent of missing direct estimates over the 14 year study period.

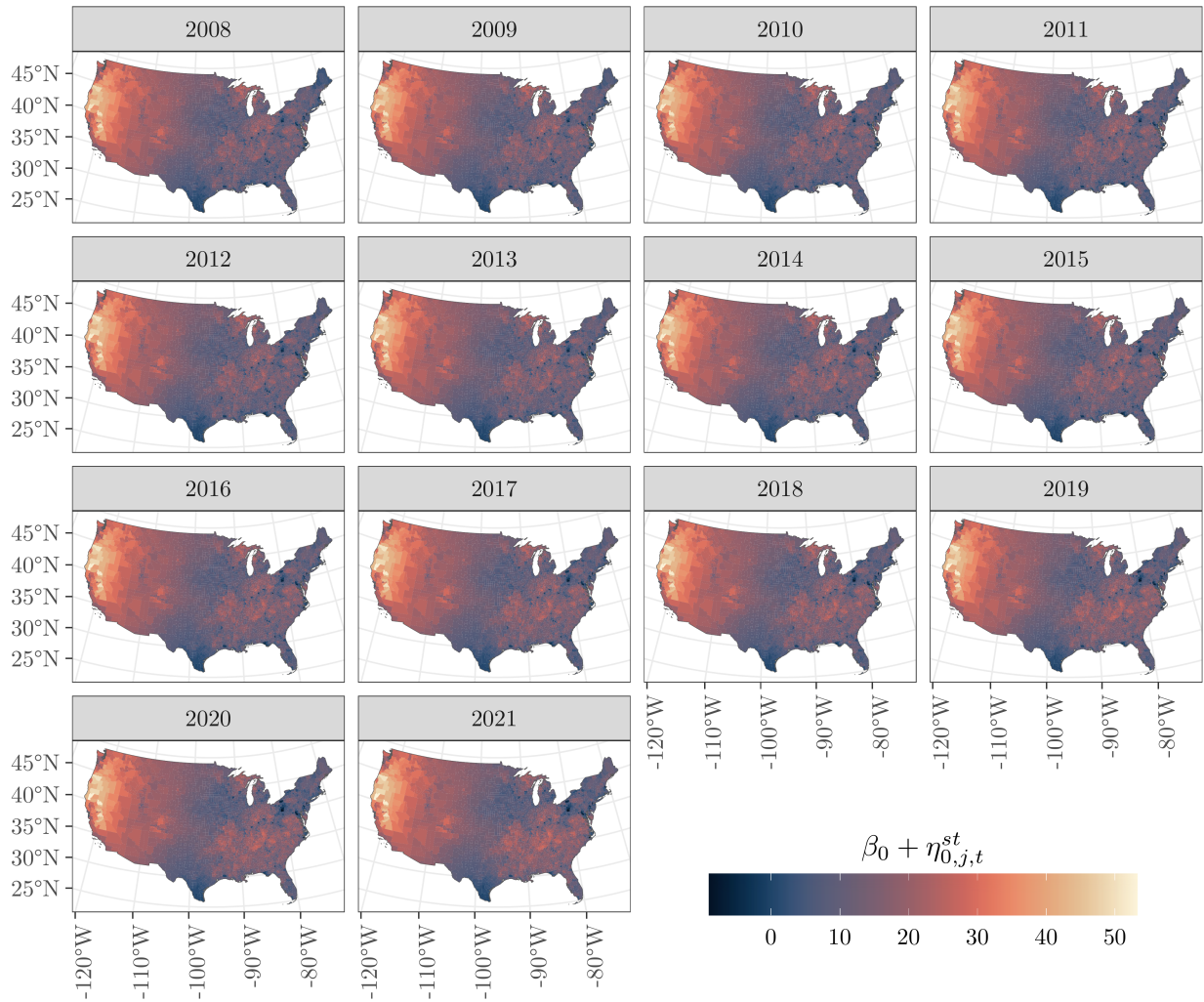


Figure S16: Posterior median of the Full model's time- and space-varying intercept $\beta_0 + \eta_{0,j,t}^{st}$ fit with FIA data.

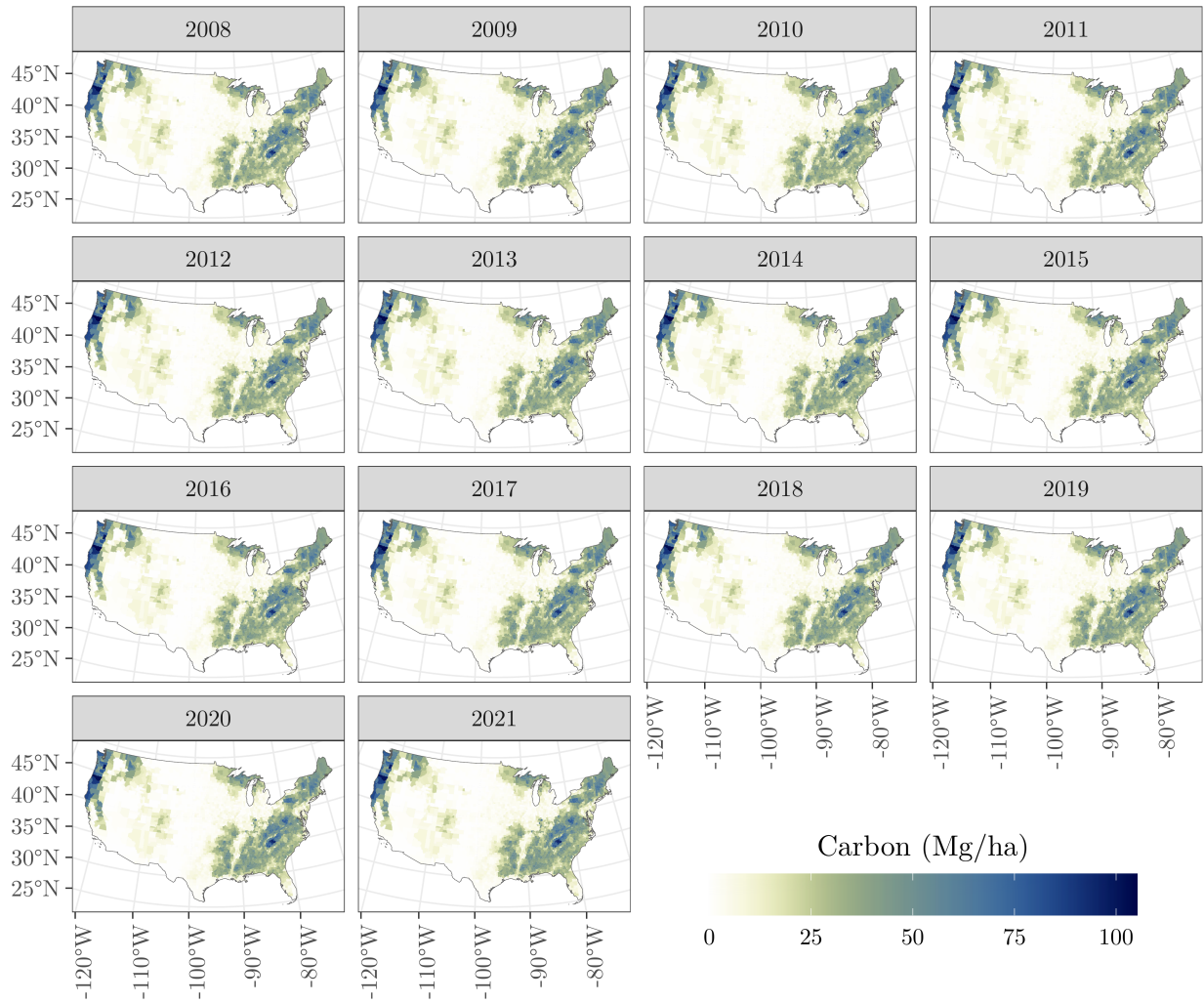


Figure S17: Full model estimates for $\mu_{j,t}$'s posterior mean fit with FIA data.

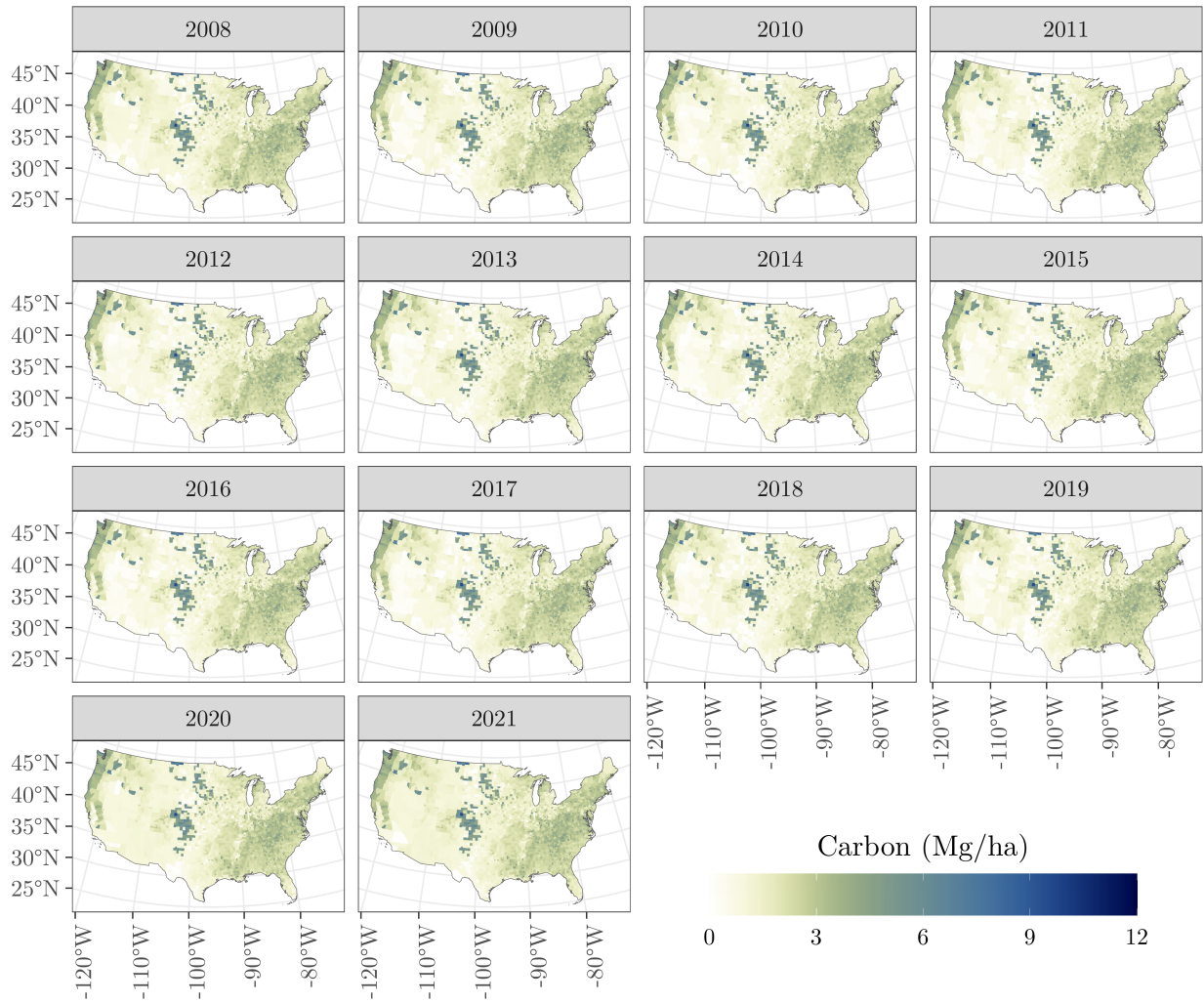


Figure S18: Full model estimates for $\mu_{j,t}$'s posterior standard deviation fit with FIA data.

Decreasing			Increasing		
State	County	Carbon	State	County	Carbon
Idaho	Idaho	-0.92 (-1.41, -0.45)	Maine	Aroostook	0.71 (0.35, 1.05)
California	Siskiyou	-0.92 (-1.33, -0.48)	Minnesota	St. Louis	0.64 (0.34, 0.96)
California	Shasta	-0.7 (-0.98, -0.44)	Maine	Piscataquis	0.57 (0.31, 0.83)
Washington	Okanogan	-0.69 (-1.00, -0.36)	Maine	Penobscot	0.49 (0.29, 0.68)
Oregon	Douglas	-0.47 (-0.87, -0.11)	Maine	Washington	0.46 (0.26, 0.64)
California	Mariposa	-0.45 (-0.60, -0.29)	Maine	Somerset	0.44 (0.22, 0.66)
California	Tuolumne	-0.45 (-0.61, -0.28)	Alabama	Baldwin	0.29 (0.19, 0.40)
California	Lake	-0.43 (-0.56, -0.30)	Maine	Hancock	0.27 (0.14, 0.40)
California	Trinity	-0.43 (-0.67, -0.20)	Minnesota	Cook	0.25 (0.08, 0.43)
California	Fresno	-0.42 (-0.73, -0.11)	Minnesota	Itasca	0.24 (0.07, 0.42)

Table S5: Ten largest decreasing and increasing estimates of total carbon trends $A_j\theta_j$ (Tg/year) from 2008 to 2021 across the CONUS, where A_j is the area of county j in hectares. Estimates are posterior medians with 95% credible interval values given in parentheses.

FIA Region	Trend $A_{\mathcal{J}}\theta_{\mathcal{J}}$ (Tg/year)	Change $A_{\mathcal{J}}\Delta_{\mathcal{J}}$ (Tg)
Northern	-1.94 (-6.74, 3.42)	43.03 (-43.05, 137.98)
Pacific Northwest	-9.55 (-14.71, -5.34)	-101.01 (-186.91, -23.12)
Rocky Mountain	-12.86 (-19.46, -6.13)	-137.03 (-285.29, -1.29)
Southern	44.32 (36.83, 50.55)	660.45 (534.73, 781.08)

Table S6: Left column, Full model estimates of total carbon trend by FIA region from 2008 and 2021, where $A_{\mathcal{J}}$ is the area of region \mathcal{J}^{th} in hectares and $\theta_{\mathcal{J}}$ is carbon trend (Tg/ha/year) as defined in (16). Right column, Full model estimates of total carbon change by FIA region between $t_1=2008$ and $t_2=2021$, where $\Delta_{\mathcal{J}}$ is carbon change (Tg/ha). Estimates are posterior medians with 95% credible intervals values given in parentheses. These trend and change estimates summarize patterns seen in Figure 6.

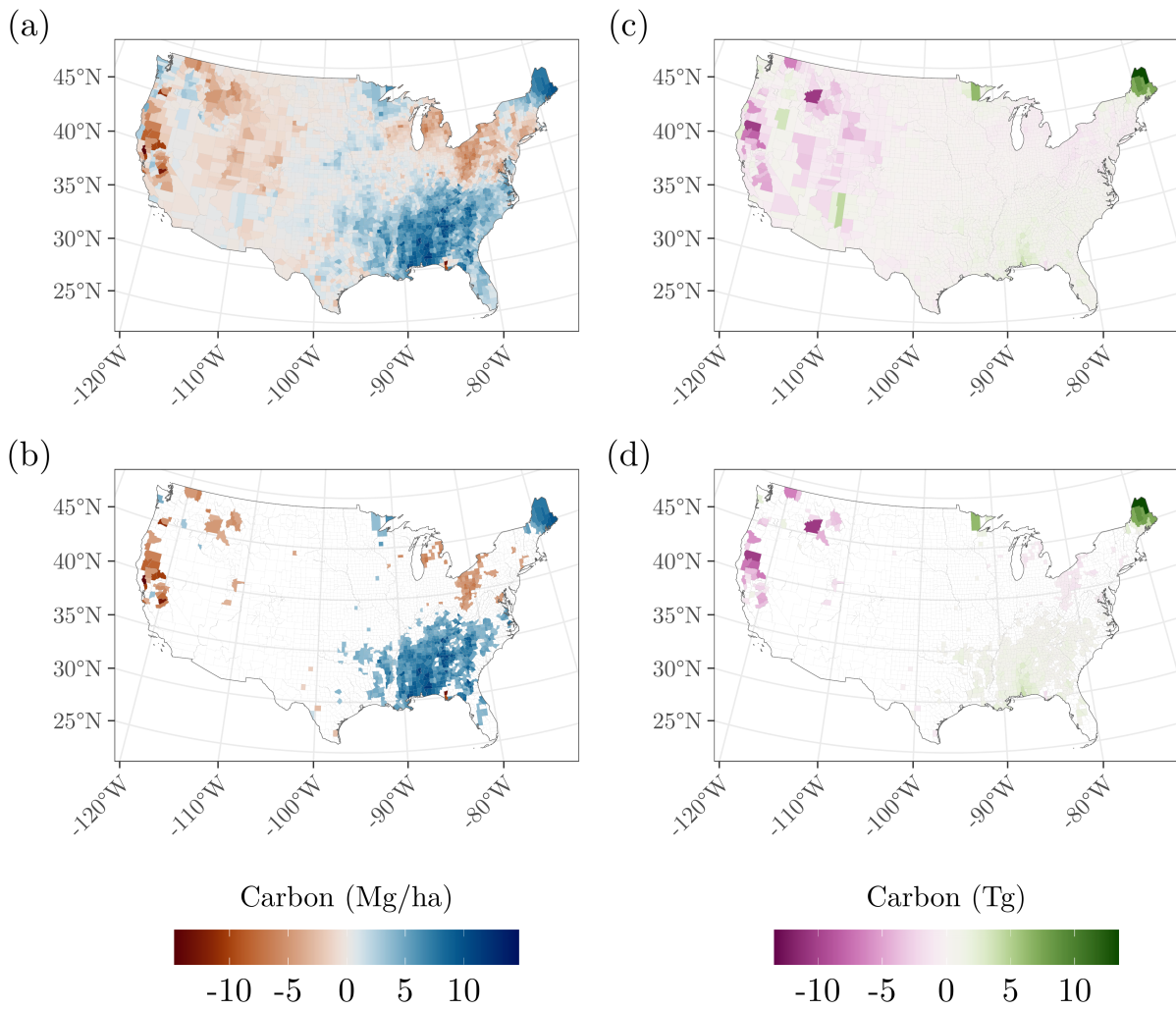


Figure S19: (a) Estimated change in forest carbon density between 2021 and 2008 Δ_j (Mg/ha). Values are each county's posterior distribution median. (b) Counties from (a) that have posterior distribution 95% credible intervals that exclude zero. (c) Estimated change in forest carbon total $A_j\Delta_j$ (Tg), where A_j is the j^{th} county's area in hectares. (d) Counties from (c) that have posterior distribution 95% credible intervals that exclude zero.

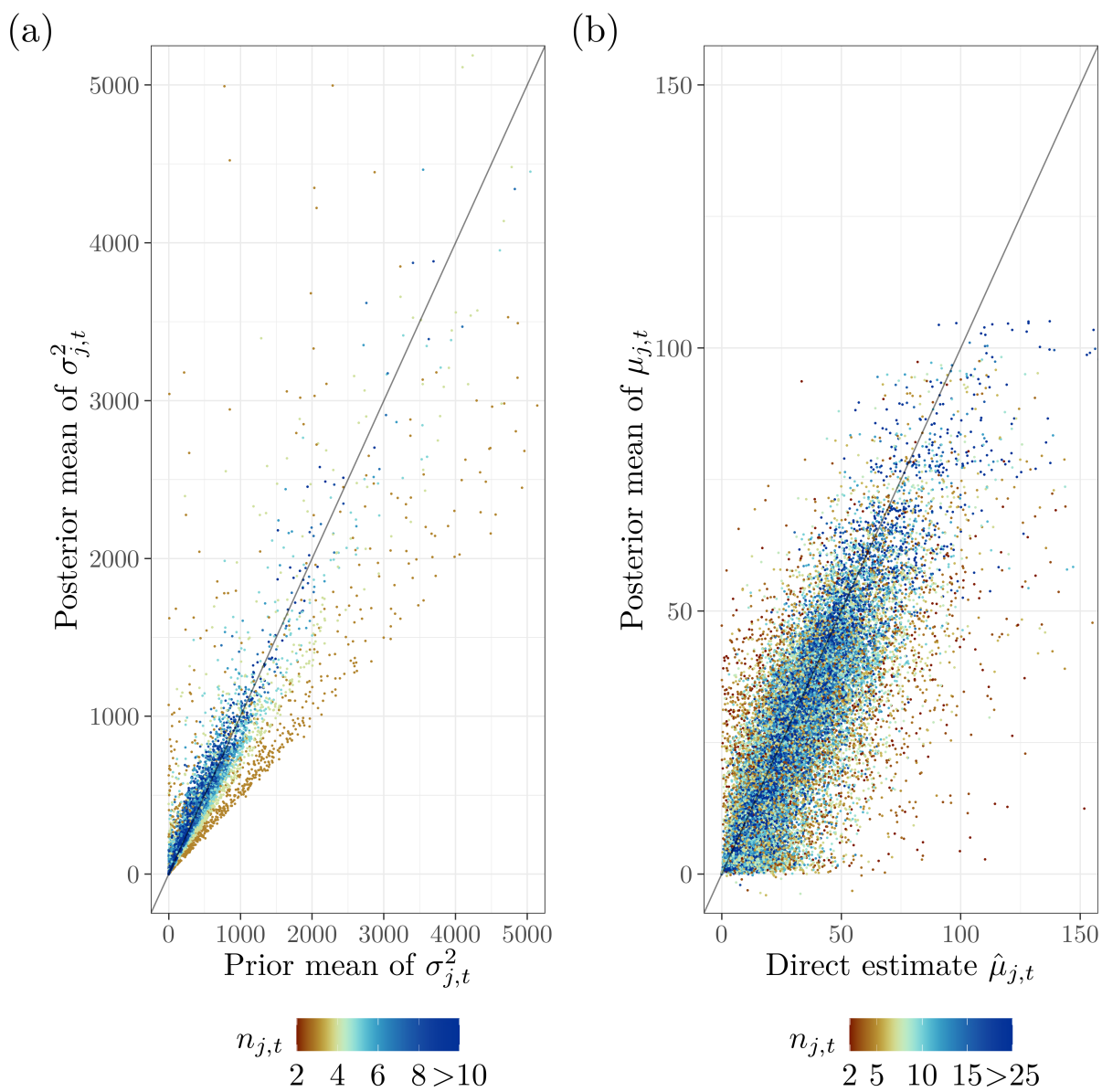


Figure S20: FIA data Full model estimates. (a) $\sigma_{j,t}^2$ prior mean versus its posterior mean. (b) $\mu_{j,t}$ direct estimate versus its posterior mean. Points colored by sample size.

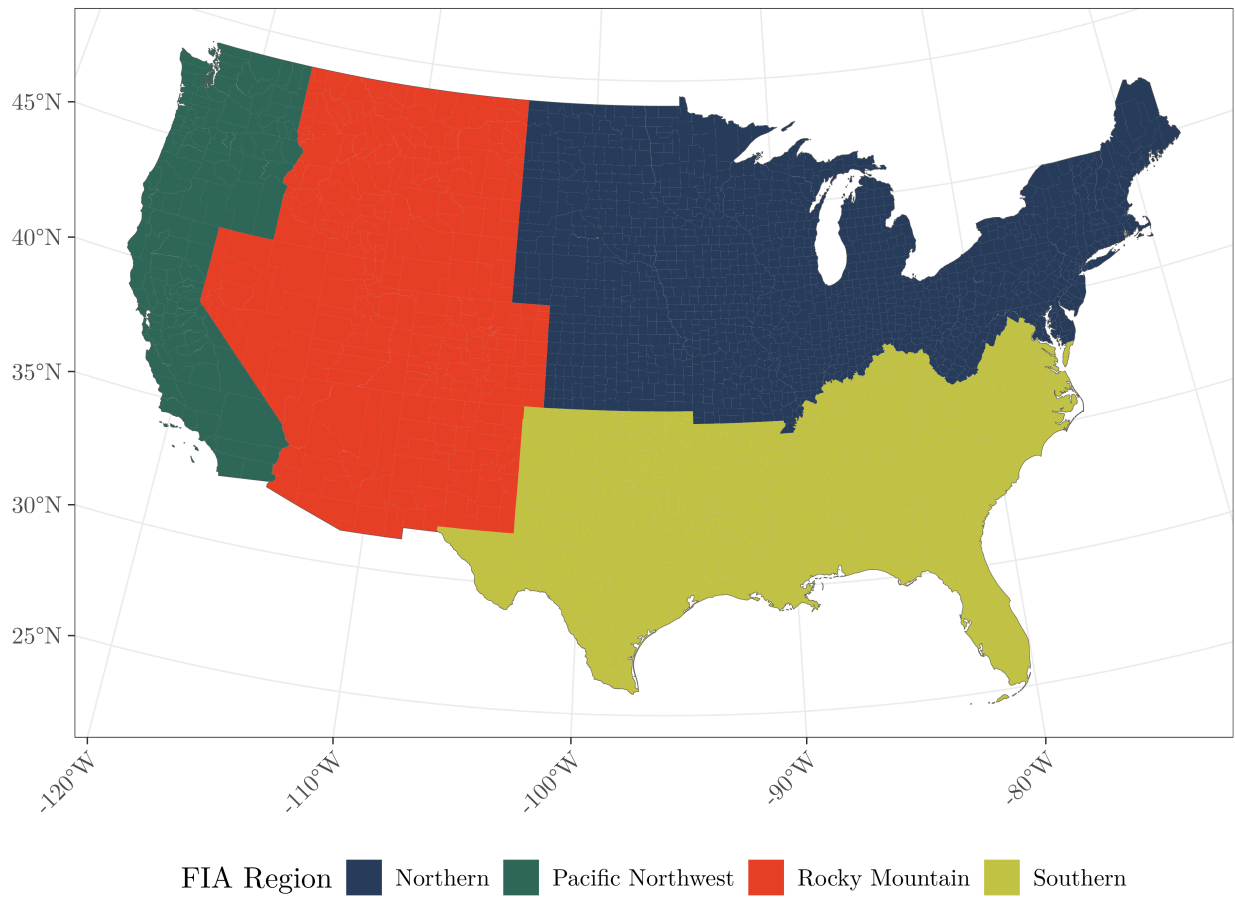


Figure S21: FIA regions used to compute county aggregate total, trend, and change estimates given in Figure 6 and Table S6.

S6.1 County specific figures

Figures comparable to Figure 5 for all counties are provided at <https://drive.google.com/drive/folders/1seksf153roVI6gFsiUKjr704Dk2Ru1xC?usp=sharing>. Upon acceptance, these figures will be moved to a permanent repository.

S7 Data and code

Data and code to reproduce results are provided at <https://drive.google.com/drive/folders/1seksf153roVI6gFsiUKjr704Dk2Ru1xC?usp=sharing>. Upon acceptance, these figures will be moved to a permanent repository.

S8 MCMC sampler and computing notes

Here we provide the MCMC sampler for the full model defined in (8).

To ease notation, we move from the double indexing notation used in the main text to a single index notation. Specifically, we define the indexing set $i = 1, \dots, N$, which directly maps to the double indexing set (j, t) defined in Section (2.1), whereby variables are ordered by time $t = 1, \dots, T$ within county $j = 1, \dots, J$. Following this new notation, let $\boldsymbol{\mu} = (\mu_1, \dots, \mu_N)^\top$ be the length N vector of latent means and $\hat{\boldsymbol{\mu}} = (\hat{\mu}_1, \dots, \hat{\mu}_N)^\top$ be the corresponding length N vector of direct estimates. Let \mathbf{X} be the $N \times (p + 1)$ design matrix with rows corresponding to the ordering of $\boldsymbol{\mu}$ and columns corresponding to an intercept and p many predictors $(\mathbf{1}, \mathbf{x}_1, \dots, \mathbf{x}_p)$, where $\mathbf{1}$ is a column of ones and $\mathbf{x}_k = (x_{k,1}, \dots, x_{k,N})^\top$ for $k = 1, \dots, p$. We then define the corresponding length $p + 1$ coefficient vector $\boldsymbol{\beta} = (\beta_0, \dots, \beta_p)^\top$. Let $\boldsymbol{\eta}_0^{st} = (\eta_{0,1}^{st}, \dots, \eta_{0,N}^{st})^\top$ be the length N vector corresponding to the spatial-temporal random intercept. Let $\boldsymbol{\eta}^s$ be the length Jq vector of random effects, with $\boldsymbol{\eta}^s = (\eta_{1,1}^s, \dots, \eta_{q,1}^s, \dots, \eta_{1,J}^s, \dots, \eta_{q,J}^s)^\top$. To update the elements of $\boldsymbol{\eta}^s$, we define q many length J sub-vectors, $(\boldsymbol{\eta}_1^s, \dots, \boldsymbol{\eta}_q^s)$, where $\boldsymbol{\eta}_k^s = (\eta_{k,1}^s, \dots, \eta_{k,J}^s)^\top$ for $k = 1, \dots, q$. We define the length $J(q - 1)$ vector $\boldsymbol{\eta}_{-k}^s$ to be $\boldsymbol{\eta}^s$ with the elements of $\boldsymbol{\eta}_k^s$ removed. To replicate the elements of $\boldsymbol{\eta}^s$ over time, we define the $Nq \times Jq$ design (indicator) matrix $\mathbf{Z} = \mathbf{I} \otimes \mathbf{1}$, where \mathbf{I} is a $Jq \times Jq$ identity matrix and $\mathbf{1}$ is a length T column vector of ones. Additionally, we define $\mathbf{Z}_k = \mathbf{I} \otimes \mathbf{1}$ where \mathbf{I} is a $J \times J$ identity matrix and $\mathbf{1}$ is a length T column vector of ones and $\mathbf{Z}_{-k} = \mathbf{I} \otimes \mathbf{1}$ where \mathbf{I} is a $J(q - 1) \times J(q - 1)$ identity matrix and $\mathbf{1}$ is a length T column vector of ones. Finally, we let $\tilde{\mathbf{X}}$ be the $N \times Nq$ block diagonal design matrix of spatially-varying predictors. Specifically, the i -th block is the length q vector $(\tilde{x}_{1,i}, \dots, \tilde{x}_{q,i})$. Accordingly, we define $\tilde{\mathbf{X}}_k$ to be the $N \times N$ diagonal matrix with elements $(\tilde{x}_{k,1}, \dots, \tilde{x}_{k,N})$ for $k = 1, \dots, q$, and $\tilde{\mathbf{X}}_{-k}$ to be the $N \times N(q - 1)$ block diagonal matrix with blocks equal to those in $\tilde{\mathbf{X}}$ with the k^{th} element removed. The full model in (8) may then be written as

$$\boldsymbol{\mu} \sim MVN(\boldsymbol{\eta}_0^{st} + \mathbf{X}\boldsymbol{\beta} + \tilde{\mathbf{X}}\mathbf{Z}\boldsymbol{\eta}^s, \sigma_\epsilon \mathbf{I}) \quad (\text{S24})$$

and update parameters as follows.

1. Update elements of $\boldsymbol{\mu}$, where corresponding $\hat{\mu}_i$ and $\hat{\sigma}_{i_{\tilde{\mathbf{X}}}}^2$ (hence σ_i^2) are available, using $\boldsymbol{\mu} | \cdot \sim MVN(\mathbf{V}\mathbf{v}, \mathbf{V})$ where $\mathbf{v} = \boldsymbol{\Sigma}_\mu^{-1} \hat{\boldsymbol{\mu}} + (\boldsymbol{\eta}_0^{st} + \mathbf{X}\boldsymbol{\beta} + \tilde{\mathbf{X}}\mathbf{Z}\boldsymbol{\eta}^s) / \sigma_\epsilon^2$, $\mathbf{V}^{-1} = (\boldsymbol{\Sigma}_\mu^{-1} + \sigma_\epsilon^{-2} \mathbf{I})$,

and Σ_μ is diagonal with diagonal elements σ_i^2 s. Vector and matrix dimensions are adjusted accordingly to remove rows corresponding to missing values. Note, \mathbf{V} is diagonal so, for efficiency, sampling should be done using a univariate normal.

2. Update elements of $\boldsymbol{\mu}$, where either corresponding $\hat{\mu}_i$ or $\hat{\sigma}_i^2$ is **not** available, using $\boldsymbol{\mu} | \cdot \sim MVN(\boldsymbol{\eta}_0^{st} + \mathbf{X}\boldsymbol{\beta} + \tilde{\mathbf{X}}\mathbf{Z}\boldsymbol{\eta}^s, \sigma_\epsilon^2\mathbf{I})$. Vector and matrix dimensions are adjusted accordingly to include rows corresponding to missing values. Note, the variance is diagonal so, for efficiency, sampling should be done using a univariate normal.
3. Update $\boldsymbol{\beta}$ using $\boldsymbol{\beta} | \cdot \sim MVN(\mathbf{V}\mathbf{v}, \mathbf{V})$ where $\mathbf{v} = \left(\Sigma_\beta^{-1} \boldsymbol{\mu}_\beta + \mathbf{X}^\top (\boldsymbol{\mu} - \boldsymbol{\eta}_0^{st} - \tilde{\mathbf{X}}\mathbf{Z}\boldsymbol{\eta}^s) / \sigma_\epsilon^2 \right)$, $\mathbf{V}^{-1} = (\Sigma_\beta^{-1} + \mathbf{X}^\top \mathbf{X} / \sigma_\epsilon^2)$ and $\Sigma_\beta = \sigma_\beta^2 \mathbf{I}$.
4. Update $\boldsymbol{\eta}_0^{st}$ using $\boldsymbol{\eta}_0^{st} | \cdot \sim MVN(\mathbf{V}\mathbf{v}, \mathbf{V})$ where $\mathbf{v} = (\boldsymbol{\mu} - \mathbf{X}\boldsymbol{\beta} - \tilde{\mathbf{X}}\mathbf{Z}\boldsymbol{\eta}^s) / \sigma_\epsilon^2$ and $\mathbf{V}^{-1} = \sigma_{\eta_0^{st}}^{-2} \mathbf{R}(\rho_{\eta_0^{st}})^{-1} \otimes \mathbf{A}(\alpha_{\eta_0^{st}})^{-1} + \sigma_\epsilon^{-2} \mathbf{I}$.
5. Update $\boldsymbol{\eta}_k^s$ for $k = 1, \dots, q$ using $\boldsymbol{\eta}_k^s | \cdot \sim MVN(\mathbf{V}\mathbf{v}, \mathbf{V})$ where $\mathbf{v} = (\tilde{\mathbf{X}}_k \mathbf{Z}_k)^\top (\boldsymbol{\mu} - \boldsymbol{\eta}_0^{st} - \mathbf{X}\boldsymbol{\beta} - \tilde{\mathbf{X}}_{-k} \mathbf{Z}_{-k} \boldsymbol{\eta}_{-k}^s) / \sigma_\epsilon^2$ and $\mathbf{V}^{-1} = \sigma_{\eta_k^s}^{-2} \mathbf{R}(\rho_{\eta_k^s})^{-1} + \sigma_\epsilon^{-2} (\tilde{\mathbf{X}}_k \mathbf{Z}_k)^\top (\tilde{\mathbf{X}}_k \mathbf{Z}_k)$.
6. Update σ_i^2 for i where both $\hat{\mu}_i$ and $\hat{\sigma}_i^2$ are available using $\sigma_i^2 | \cdot \sim IG(a, b)$ where $a = n_i/2 + 1/2$ and $b = (n_i - 1)\hat{\sigma}_i^2/2 + (\hat{\mu}_i - \mu_i)^2/2$.
7. Update $\sigma_{\eta_0^{st}}^2$ using $\sigma_{\eta_0^{st}}^2 | \cdot \sim IG(a, b)$ where $a = a_{\eta_0^{st}} + N/2$ and $b = b_{\eta_0^{st}} + (\boldsymbol{\eta}_0^{st\top} (\mathbf{R}(\rho_{\eta_0^{st}}) \otimes \mathbf{A}(\alpha_{\eta_0^{st}}))^{-1} \boldsymbol{\eta}_0^{st})/2$.
8. Update $\sigma_{\eta_k^s}^2$ for $k = 1, \dots, q$ using $\sigma_{\eta_k^s}^2 | \cdot \sim IG(a, b)$ where $a = a_{\eta_k^s} + J/2$ and $b = b_{\eta_k^s} + \boldsymbol{\eta}_k^{s\top} \mathbf{R}(\rho_{\eta_k^s})^{-1} \boldsymbol{\eta}_k^s$.
9. Update σ_ϵ^2 using $\sigma_\epsilon^2 | \cdot \sim IG(a, b)$ where $a = a_\epsilon + N/2$ and $b = b_\epsilon + (\boldsymbol{\eta}_0^{st} + \mathbf{X}\boldsymbol{\beta} + \tilde{\mathbf{X}}\mathbf{Z}\boldsymbol{\eta}^s)^\top (\boldsymbol{\eta}_0^{st} + \mathbf{X}\boldsymbol{\beta} + \tilde{\mathbf{X}}\mathbf{Z}\boldsymbol{\eta}^s) / 2$.
10. Jointly update $\rho_{\eta_0^{st}}$ and $\alpha_{\eta_0^{st}}$ using the Metropolis algorithm with log target density plus Jacobian adjustment for the Uniform prior distribution proportional to

$$-1/2 \log |\sigma_{\eta_0^{st}}^2 \mathbf{R}(\rho_{\eta_0^{st}}) \otimes \mathbf{A}(\alpha_{\eta_0^{st}})| - 1/2 \boldsymbol{\eta}_0^{st\top} (\sigma_{\eta_0^{st}}^2 \mathbf{R}(\rho_{\eta_0^{st}}) \otimes \mathbf{A}(\alpha_{\eta_0^{st}}))^{-1} \boldsymbol{\eta}_0^{st} + \log(\alpha_{\eta_0^{st}} - a_\alpha) + \log(b_\alpha - \alpha_{\eta_0^{st}}) + \log(\rho_{\eta_0^{st}} - a_\rho) + \log(b_\rho - \rho_{\eta_0^{st}}).$$
11. Update $\rho_{\eta_k^s}$ for $k = 1, \dots, q$ using the Metropolis algorithm with log target density plus Jacobian adjustment for the Uniform prior distribution proportional to

$$-1/2 \log |\sigma_{\eta_k^s}^2 \mathbf{R}(\rho_{\eta_k^s})| - 1/2 \boldsymbol{\eta}_k^{s\top} (\sigma_{\eta_k^s}^2 \mathbf{R}(\rho_{\eta_k^s}))^{-1} \boldsymbol{\eta}_k^s + \log(\rho_{\eta_k^s} - a_\rho) + \log(b_\rho - \rho_{\eta_k^s}).$$

To efficiently evaluate the CAR precision matrix $\mathbf{R}(\rho_{\eta^s})^{-1}$ defined in Section 2.2, we define $\mathbf{R}(\rho_{\eta^s})^{-1} = (\mathbf{D} - \rho_{\eta^s} \mathbf{W}) = \mathbf{D}^{1/2} (\mathbf{I} - \rho_{\eta^s} \mathbf{D}^{-1/2} \mathbf{W} \mathbf{D}^{-1/2}) \mathbf{D}^{1/2}$, where \mathbf{I} is the $J \times J$ identity matrix, and let $\mathbf{D}^{-1/2} \mathbf{W} \mathbf{D}^{-1/2} = \mathbf{P} \boldsymbol{\Lambda} \mathbf{P}^\top$ where $\boldsymbol{\Lambda}$ is the diagonal matrix of eigenvalues and the columns of \mathbf{P} are the eigenvectors of $\mathbf{D}^{-1/2} \mathbf{W} \mathbf{D}^{-1/2}$. This allows $\mathbf{R}(\rho_{\eta^s})^{-1}$ to be expressed

as $\sum_{i=1}^J (1 - \rho_{\eta^s} \lambda_i) \mathbf{v}_i \mathbf{v}_i^\top = \sum_{i=1}^J \mathbf{v}_i \mathbf{v}_i^\top - \rho_{\eta^s} (\sum_{i=1}^J \lambda_i \mathbf{v}_i \mathbf{v}_i^\top)$, where \mathbf{v}_i are the columns of $\mathbf{D}^{1/2} \mathbf{P}$ and λ_i are the diagonal elements of $\mathbf{\Lambda}$. Expressing the precision matrix in this way removes the need for costly matrix formation and Cholesky decomposition in each MCMC iteration. Rather, the first term, i.e., $\sum_{i=1}^J \mathbf{v}_i \mathbf{v}_i^\top$, remains the same across MCMC iterations and the second term, i.e., $\rho_{\eta^s} (\sum_{i=1}^J \lambda_i \mathbf{v}_i \mathbf{v}_i^\top)$, only varies by a multiplicative constant ρ_{η^s} . Further, the determinant of $\mathbf{R}(\rho_{\eta^s})^{-1}$, which is needed to update correlation parameters ρ_{η^s} and $\rho_{\eta_0^{st}}$ via Metropolis steps, is simplified to $\prod_{i=1}^J \mathbf{D}_{ii} (1 - \rho_{\eta^s} \lambda_i)$, which requires no linear algebra across MCMC iterations.

In Steps 3, 4, and 5 we sample from $MVN(\mathbf{V}\mathbf{v}, \mathbf{V})$ which is most efficiently accomplished via $\mathbf{U}^{-1}\mathbf{b}$ where $\mathbf{b} = \mathbf{U}^{-\top} \mathbf{v} + \mathbf{a}$, \mathbf{U} is the upper-triangular Cholesky square root of \mathbf{V}^{-1} and \mathbf{a} is a vector of realizations from a standard normal distribution $N(0, 1)$.

In step 10, we utilize matrix sparseness and properties of Kronecker products and determinants to compute $\log(|\sigma_{\eta_0^{st}}^2 \mathbf{R}(\rho_{\eta_0^{st}}) \otimes \mathbf{A}(\alpha_{\eta_0^{st}})|)$. Let $\mathbf{A}(\alpha_{\eta_0^{st}}) = \mathbf{B}\mathbf{B}^\top$ be the Cholesky decomposition of $\mathbf{A}(\alpha_{\eta_0^{st}})$, with \mathbf{b} as the vector of diagonal elements of \mathbf{B} . Also, let \mathbf{d} and $\boldsymbol{\lambda}$ be the vectors of diagonal elements of the matrices \mathbf{D} and $\mathbf{\Lambda}$ defined previously. We then have

$$\begin{aligned} \log |\sigma_{\eta_0^{st}}^2 \mathbf{R}(\rho_{\eta_0^{st}}) \otimes \mathbf{A}(\alpha_{\eta_0^{st}})| &= \log(|\mathbf{A}(\alpha_{\eta_0^{st}})|^J \times |\sigma_{\eta_0^{st}}^2 \mathbf{R}(\rho_{\eta_0^{st}})|^T) \\ &= J \log |\mathbf{A}(\alpha_{\eta_0^{st}})| + T \log |\sigma_{\eta_0^{st}}^2 \mathbf{R}(\rho_{\eta_0^{st}})| \\ &= 2J \sum \log \mathbf{b} - T \log |1/\sigma_{\eta_0^{st}}^2 \mathbf{R}(\rho_{\eta_0^{st}})^{-1}| \\ &= 2J \sum \log \mathbf{b} - T(J \log(1/\sigma_{\eta_0^{st}}^2) + \log |\mathbf{R}(\rho_{\eta_0^{st}})^{-1}|) \\ &= 2J \sum \log \mathbf{b} - N \log(1/\sigma_{\eta_0^{st}}^2) - T \sum \log(\mathbf{d} \odot (1 - \rho_{\eta_0^{st}} \boldsymbol{\lambda})), \end{aligned}$$

where \odot denotes element-wise multiplication.

In step 11, we again use the same identities to efficiently evaluate $\log |\sigma_{\eta_k^s}^2 \mathbf{R}(\rho_{\eta_k^s})|$ as

$$\begin{aligned} \log |\sigma_{\eta_k^s}^2 \mathbf{R}(\rho_{\eta_k^s})| &= -\log |1/\sigma_{\eta_k^s}^2 \mathbf{R}(\rho_{\eta_k^s})^{-1}| \\ &= -J \log(1/\sigma_{\eta_k^s}^2) - \sum \log(\mathbf{d} \odot (1 - \rho_{\eta_k^s} \boldsymbol{\lambda})). \end{aligned}$$

Acknowledgements

This work was supported by the USDA Forest Service, NSF DEB-2213565, and NASA CMS grants Hayes (CMS 2020). The findings and conclusions in this publication are those of the author(s) and should not be construed to represent any official US Department of Agriculture or US Government determination or policy.

References

Affleck, D. L. and Gaines III, G. C. (2023). Model-assisted domain estimation of postfire tree regeneration in the western us using nearest neighbor techniques. *Canadian Journal of Forest Research*, 53(12):981–995.

- Banerjee, S. (2024). Finite population survey sampling: An unapologetic bayesian perspective. *Sankhya A*.
- Banerjee, S., Carlin, B., and Gelfand, A. (2004). *Hierarchical Modeling and Analysis of Spatial Data*, volume 101. Chapman & Hall/CRC Monographs on Statistical and Applied Probability;.
- Bates, D., Maechler, M., and Jagan, M. (2023). *Matrix: Sparse and Dense Matrix Classes and Methods*. R package version 1.6-1.
- Bechtold, W. A. and Patterson, P. L., editors (2005). *The enhanced forest inventory and analysis program: national sampling design and estimation procedures*. U.S. Department of Agriculture, Forest Service, Southern Research Station, Asheville, NC.
- Breidenbach, J. and Astrup, R. (2012). Small area estimation of forest attributes in the Norwegian National Forest Inventory. *European Journal of Forest Research*, 131(4):1255–1267.
- Breidt, F. J. and Opsomer, J. D. (2017). Model-assisted survey estimation with modern prediction techniques. *Statistical Science*, 32(2):190–205.
- Cao, Q., Dettmann, G. T., Radtke, P. J., Coulston, J. W., Derwin, J., Thomas, V. A., Burkhart, H. E., and Wynne, R. H. (2022). Increased precision in county-level volume estimates in the united states national forest inventory with area-level small area estimation. *Frontiers in Forests and Global Change*, 5.
- Chandra, H., Salvati, N., and Chambers, R. (2015). A spatially nonstationary Fay-Herriot model for small area estimation. *Journal of Survey Statistics and Methodology*, 3(2):109–135.
- Coulston, J. W., Green, P. C., Radtke, P. J., Prisley, S. P., Brooks, E. B., Thomas, V. A., Wynne, R. H., and Burkhart, H. E. (2021). Enhancing the precision of broad-scale forest-land removals estimates with small area estimation techniques. *Forestry: An International Journal of Forest Research*, 94(3):427–441.
- Cressie, N. and Wikle, C. (2011). *Statistics for Spatio-Temporal Data*. CourseSmart Series. Wiley.
- Datta, A., Banerjee, S., Finley, A. O., and Gelfand, A. E. (2016). Hierarchical nearest-neighbor gaussian process models for large geostatistical datasets. *Journal of the American Statistical Association*, 111(514):800–812.
- Domke, G. M., Walters, B. F., Giebink, C. L., Greenfield, E. J., Smith, J. E., Nichols, M. C., Knott, J. A., Ogle, S. M., Coulston, J. W., and Steller, J. (2023). *Greenhouse gas emissions and removals from forest land, woodlands, urban trees, and harvested wood products in the United States, 1990-2021*.

- Doser, J. W., Finley, A. O., Saunders, S. P., Kéry, M., Weed, A. S., and Zipkin, E. F. (2024). Modeling complex species-environment relationships through spatially-varying coefficient occupancy models. *Journal of Agricultural, Biological and Environmental Statistics*.
- Dumelle, M., Higham, M., Ver Hoef, J. M., Olsen, A. R., and Madsen, L. (2022). A comparison of design-based and model-based approaches for finite population spatial sampling and inference. *Methods in Ecology and Evolution*, 13(9):2018–2029.
- Fay, R. E. and Herriot, R. A. (1979). Estimates of income for small places: An application of james-stein procedures to census data. *Journal of the American Statistical Association*, 74(366).
- Finley, A. O., Andersen, H.-E., Babcock, C., Cook, B. D., Morton, D. C., and Banerjee, S. (2024). Models to support forest inventory and small area estimation using sparsely sampled lidar: A case study involving g-liht lidar in tanana, alaska. *Journal of Agricultural, Biological and Environmental Statistics*.
- Finley, A. O., Banerjee, S., and MacFarlane, D. W. (2011). A hierarchical model for quantifying forest variables over large heterogeneous landscapes with uncertain forest areas. *Journal of the American Statistical Association*, 106(493):31–48.
- Gelman, A., Carlin, J., Stern, H., Dunson, D., Vehtari, A., and Rubin, D. (2013). *Bayesian Data Analysis, Third Edition*. Chapman & Hall/CRC Texts in Statistical Science. Taylor & Francis.
- Ghosh, M. (2012). Finite population sampling: A model-design synthesis. *Statistics in Transition new series*, 13(2):235–242.
- Ghosh, M., Ghosh, T., and Hirose, M. Y. (2022). Poisson counts, square root transformation and small area estimation. *Sankhya B*, 84(2):449–471.
- Gregoire, T. G. (1998). Design-based and model-based inference in survey sampling: appreciating the difference. *Canadian Journal of Forest Research*, 28(10):1429–1447.
- Harris, N. L., Hagen, S. C., Saatchi, S. S., Pearson, T. R. H., Woodall, C. W., Domke, G. M., Braswell, B. H., Walters, B. F., Brown, S., Salas, W., Fore, A., and Yu, Y. (2016). Attribution of net carbon change by disturbance type across forest lands of the conterminous united states. *Carbon Balance and Management*, 11(1):24.
- Hogan, J. A., Domke, G. M., Zhu, K., Johnson, D. J., and Lichstein, J. W. (2024). Climate change determines the sign of productivity trends in us forests. *Proceedings of the National Academy of Sciences*, 121(4).
- Hoover, C. M. and Smith, J. E. (2021). Current aboveground live tree carbon stocks and annual net change in forests of conterminous united states. *Carbon Balance and Management*, 16(1):17.

- Hou, Z., Domke, G. M., Russell, M. B., Coulston, J. W., Nelson, M. D., Xu, Q., and McRoberts, R. E. (2021). Updating annual state-and county-level forest inventory estimates with data assimilation and FIA data. *Forest Ecology and Management*, 483:118777.
- Housman, I., Schleeweis, K., Heyer, J., Ruefenacht, B., Bender, S., Megown, K., Goetz, W., and Bogle, S. (2023). National land cover database tree canopy cover methods v2021.4. GTAC-10268-RPT1. Salt Lake City, UT: U.S. Department of Agriculture, Forest Service, Geospatial Technology and Applications Center.
- IPCC (2019). Climate Change and Land: an IPCC special report on climate change, desertification, land degradation, sustainable land management, food security, and greenhouse gas fluxes in terrestrial ecosystems. Edited by P.R. Shukla, J. Skea, E. Calvo Buendia, V. Masson-Delmotte, H.-O. Pörtner, D. C. Roberts, P. Zhai, R. Slade, S. Connors, R. van Diemen, M. Ferrat, E. Haughey, S. Luz, S. Neogi, M. Pathak, J. Petzold, J. Portugal Pereira, P. Vyas, E. Huntley, K. Kissick, M. Belkacemi, J. Malley.
- Knott, J. A., Liknes, G. C., Giebink, C. L., Oh, S., Domke, G. M., McRoberts, R. E., Quirino, V. F., and Walters, B. F. (2023). Effects of outliers on remote sensing-assisted forest biomass estimation: A case study from the united states national forest inventory. *Methods in Ecology and Evolution*, 14(7):1587–1602.
- Köhl, M., Magnussen, S., and Marchetti, M. (2006). *Sampling methods, remote sensing and GIS multiresource forest inventory*. Springer.
- Lee, D., Rushworth, A., and Napier, G. (2018). Spatio-temporal areal unit modeling in R with conditional autoregressive priors using the CARBayesST package. *Journal of Statistical Software*, 84(9):1–39.
- Lister, A. J., Andersen, H., Frescino, T., Gatzliolis, D., Healey, S., Heath, L. S., Liknes, G. C., McRoberts, R. E., Moisen, G. G., Nelson, M., et al. (2020). Use of Remote Sensing Data to Improve the Efficiency of National Forest Inventories: A Case Study from the United States National Forest Inventory. *Forests*, 11(12):1364.
- Little, R. J. (2004). To model or not to model? Competing modes of inference for finite population sampling. *Journal of the American Statistical Association*, 99(466):546–556.
- Marhuenda, Y., Molina, I., and Morales, D. (2013). Small area estimation with spatio-temporal fay–herriot models. *Computational Statistics & Data Analysis*, 58:308–325. The Third Special Issue on Statistical Signal Extraction and Filtering.
- May, P., McConville, K. S., Moisen, G. G., Bruening, J., and Dubayah, R. (2023). A spatially varying model for small area estimates of biomass density across the contiguous united states. *Remote Sensing of Environment*, 286:113420.
- May, P. B. and Finley, A. O. (2024). Calibrating satellite maps with field data for improved predictions of forest biomass.

- McRoberts, R. E. (2010). Probability- and model-based approaches to inference for proportion forest using satellite imagery as ancillary data. *Remote Sensing of Environment*, 114(5):1017–1025.
- Porter, A. T., Holan, S. H., Wikle, C. K., and Cressie, N. (2014). Spatial fay–herriot models for small area estimation with functional covariates. *Spatial Statistics*, 10:27–42.
- Prisley, S., Bradley, J., Clutter, M., Friedman, S., Kempka, D., Rakestraw, J., and Sonne Hall, E. (2021). Needs for small area estimation: Perspectives from the us private forest sector. *Frontiers in Forests and Global Change*, 4.
- R Core Team (2023). *R: A Language and Environment for Statistical Computing*. R Foundation for Statistical Computing, Vienna, Austria.
- Rao, J. N. and Molina, I. (2015). *Small area estimation*. John Wiley & Sons.
- Rao, J. N. K. and Yu, M. (1994). Small-area estimation by combining time-series and cross-sectional data. *The Canadian Journal of Statistics / La Revue Canadienne de Statistique*, 22(4):511–528.
- Rushworth, A., Lee, D., and Mitchell, R. (2014). A spatio-temporal model for estimating the long-term effects of air pollution on respiratory hospital admissions in greater london. *Spatial and Spatio-temporal Epidemiology*, 10:29–38.
- Rushworth, A., Lee, D., and Sarran, C. (2017). An adaptive spatiotemporal smoothing model for estimating trends and step changes in disease risk. *Journal of the Royal Statistical Society. Series C (Applied Statistics)*, 66(1):141–157.
- Särndal, C., Swensson, B., and Wretman, J. (2003). *Model Assisted Survey Sampling*. Springer Series in Statistics. Springer New York.
- Särndal, C.-E., Thomsen, I., Hoem, J. M., Lindley, D. V., Barndorff-Nielsen, O., and Dalenius, T. (1978). Design-based and model-based inference in survey sampling [with discussion and reply]. *Scandinavian Journal of Statistics*, 5(1):27–52.
- Schroeder, T. A., Healey, S. P., Moisen, G. G., Frescino, T. S., Cohen, W. B., Huang, C., Kennedy, R. E., and Yang, Z. (2014). Improving estimates of forest disturbance by combining observations from Landsat time series with US Forest Service Forest Inventory and Analysis data. *Remote Sensing of Environment*, 154:61–73.
- Stanke, H., Finley, A. O., and Domke, G. M. (2022). Simplifying small area estimation with rfia: A demonstration of tools and techniques. *Frontiers in Forests and Global Change*, 5.
- Temesgen, H., Mauro, F., Hudak, A. T., Frank, B., Monleon, V., Fekety, P., Palmer, M., and Bryant, T. (2021). Using fay–herriot models and variable radius plot data to develop a stand-level inventory and update a prior inventory in the western cascades, or, united states. *Frontiers in Forests and Global Change*, 4.

- Tomppo, E., Schadauer, K., McRoberts, R. E., Gschwantner, T., Gabler, K., and Ståhl, G. (2009). *National forest inventories: pathways for common reporting (Vol. 1)*. Springer.
- Tyukavina, A., Potapov, P., Hansen, M. C., Pickens, A. H., Stehman, S. V., Turubanova, S., Parker, D., Zalles, V., Lima, A., Kommareddy, I., Song, X.-P., Wang, L., and Harris, N. (2022). Global trends of forest loss due to fire from 2001 to 2019. *Frontiers in Remote Sensing*, 3.
- UNFCCC (1992). United Nations Framework Convention On Climate Change. Secretariat of the United Nations Framework Convention on Climate Change, Bonn, Germany, 24 pp.
- Vehtari, A., Gabry, J., Magnusson, M., Yao, Y., Bürkner, P.-C., Paananen, T., and Gelman, A. (2024). loo: Efficient leave-one-out cross-validation and waic for bayesian models. R package version 2.7.0.
- Vehtari, A., Gelman, A., and Gabry, J. (2017). Practical bayesian model evaluation using leave-one-out cross-validation and waic. *Statistics and Computing*, 27(5):1413–1432.
- Ver Hoef, J. M., Peterson, E. E., Hooten, M. B., Hanks, E. M., and Fortin, M.-J. (2018). Spatial autoregressive models for statistical inference from ecological data. *Ecological Monographs*, 88(1):36–59.
- Ver Planck, N. R., Finley, A. O., Kershaw, J. A., Weiskittel, A. R., and Kress, M. C. (2018). Hierarchical bayesian models for small area estimation of forest variables using lidar. *Remote Sensing of Environment*, 204:287–295.
- Waller, L. A., Carlin, B. P., Xia, H., and Gelfand, A. E. (1997). Hierarchical spatio-temporal mapping of disease rates. *Journal of the American Statistical Association*, 92(438):607–617.
- Wang, J. C., Holan, S. H., Nandram, B., Barboza, W., Toto, C., and Anderson, E. (2012). A bayesian approach to estimating agricultural yield based on multiple repeated surveys. *Journal of Agricultural, Biological, and Environmental Statistics*, 17(1):84–106.
- Watanabe, S. (2010). Asymptotic equivalence of bayes cross validation and widely applicable information criterion in singular learning theory. *J. Mach. Learn. Res.*, 11:3571–3594.
- Westfall, J. A., Coulston, J. W., Gray, A. N., Shaw, J. D., Radtke, P. J., Walker, D. M., Weiskittel, A. R., MacFarlane, D. W., Affleck, D. L., Zhao, D., Temesgen, H., Poudel, K. P., Frank, J. M., Prisley, S. P., Wang, Y., Meador, A. J. S., Auty, D., and Domke, G. M. (2023). *A national-scale tree volume, biomass, and carbon modeling system for the United States*. Gen. Tech. Rep. WO-104. Washington, DC: U.S. Department of Agriculture, Forest Service.
- Westfall, J. A., Coulston, J. W., Moisen, G. G., and Andersen, H. E., editors (2022). Sampling and estimation documentation for the Enhanced Forest Inventory and Analysis Program: 2022. General Technical Report NRS-207, U.S. Department of Agriculture, Forest Service, Northern Research Station, Madison, WI.

- Wiener, S. S., Bush, R., Nathanson, A., Pelz, K., Palmer, M., Alexander, M. L., Anderson, D., Treasure, E., Baggs, J., and Sheffield, R. (2021). United states forest service use of forest inventory data: Examples and needs for small area estimation. *Frontiers in Forests and Global Change*, 4.
- Wojcik, O. C., Olson, S. D., Nguyen, P.-H. V., McConville, K. S., Moisen, G. G., and Frescino, T. S. (2022). Gregory: a modified generalized regression estimator approach to estimating forest attributes in the interior western us. *Frontiers in Forests and Global Change*, 4:763414.
- Wurtzebach, Z., DeRose, R. J., Bush, R. R., Goeking, S. A., Healey, S., Menlove, J., Pelz, K. A., Schultz, C., Shaw, J. D., and Witt, C. (2019). Supporting national forest system planning with forest inventory and analysis data. *Journal of Forestry*, 118(3):289–306.